Search for missing Nucleon Resonances in the Photoproduction of Hyperons using a Polarized Photon Beam and a Polarized Target

F.J. Klein[1 2], H. Crannell, R. Hakobyan, D.I. Sober
The Catholic University of America, Washington, DC 20064
L. Todor[1], R. Schumacher
Carnegie Mellon University, Pittsburgh, PA 15213
P. Eugenio[1], S. McAleer, A. Ostrovidov
Florida State University, Tallahassee, FL 32306
W.J. Briscoe, I. Strakovsky, S. Strauch, R. Workman
The George Washington University, Washington, DC 20052
J.C. Sanabria
Universidad de los Andes, A.A. 4976, Santafé de Bogotá, Colombia
E. Pasyuk
Arizona State University, Tempe, AZ 85287
C. Djalali, A. Dzyubak, D. Tedeschi, M. Wood
University of South Carolina, Columbia, SC 29208
P.L. Cole
University of Texas at El Paso, El Paso, TX 79968
D. Jenkins
Virginia Polytechnic Institute, Blacksburg, VA 24061
D.G. Crabb
University of Virginia, Charlottesville, VA 22901

+

The CLAS Collaboration

[1]Co-Spokesperson
[2]Contact person

Abstract

The long-standing question of "missing resonances", i.e. experimentally not established baryon states which are predicted by SU(6)×O(3) symmetric quark models but not expected by the di-quark model, can only be settled if measurements unambiguously identify some of these resonances. Symmetric quark models predict several "missing" baryon states to couple strongly to γp as well as $K\Lambda$ or $K\Sigma$ but not significantly to πN. Resonances with these properties would not have been observed in pion beam experiments on which most of the data analyses are based.

We propose to measure a large set of single and double polarization observables in associated strangeness production using a polarized target and polarized photon beams. The final goal of this experiment, in concert with the CLAS-g1 experiment on hyperon photoproduction (E89-004) and the **C**LAS **A**pproved **A**nalysis of $\vec{\gamma}p \to K^+\Lambda$ (as part of CLAS-g8), is to perform a complete set of measurements for ground-state hyperon photoproduction in the reactions $\gamma p \to K^+\Lambda$, $\gamma p \to K^+\Sigma^0$, and $\gamma p \to K^0\Sigma^+$. This will allow us to perform a full partial wave analysis and to determine the contributing multipoles as a function of the center-of-mass energy $W=\sqrt{s}$, thus we will extract the transition amplitudes not only of established baryon resonances but also from resonant states which are not yet experimentally observed.

Due to the weak decay of Λ and Σ^+, the **recoil** polarization can be determined in coincidence with polarization states of the incoming particles: **beam photon** and **target proton**. We will extract – for each individual reaction – more than the eight required observables which fully describe these reaction channels. The simultaneous measurement of most double polarization observables involving polarized targets will allow for powerful constraints on the fits and extensive checks of systematics. Calculations based on isobar models show that polarization observables involving beam and target polarization are most sensitive to s-channel contributions, e.g. contributions of N^* or Δ^* states.

In order to perform a complete set of measurements, we have to measure different sets of double polarization observables which can be obtained by two categories of measurements: (1) with longitudinally polarized target and circularly polarized photon beam, (2) with transversely polarized target and linearly polarized beam.

We propose to perform the measurements using the Hall-B photon beam facility and the CLAS detector which is a unique magnetic spectrometer with large acceptance, suitable for a crucial part of this experiment as it allows to operate a transversely polarized frozen spin target. The measurements will cover almost the full angular range and a large energy range: from $W = 1.705$ GeV to $W = 2.34$ GeV ($1.08 < E_\gamma < 2.5$ GeV).

While we will share the approved beam time of E01-104 **for the measurement on longitudinally polarized target, we request additional 20 days of beam time for 1.6 GeV electron beam and 20 days for 2.6 GeV electron beam.**
For the measurement on transversely polarized target and linearly polarized beam we request 38 days of beam time at $E_0 = 4.5$ GeV, probing the photon energy range between 1.2 GeV and 2.5 GeV via coherent bremsstrahlung.

1 Introduction

The detailed study and understanding of the excitation spectrum of the nucleon is required to describe the underlying interactions. The nonperturbative nature of QCD at low energies has represented a major challenge to hadronic physics, and made it unavoidable to use phenomenological quark models. In these models, the internal structure of the nucleon is represented by three constituent valence quarks interacting with each other through a potential [1, 2, 3]. The number of nucleon resonances predicted by quark models based on the SU(6)$\times$O(3) symmetry is larger than the number of the experimentally discovered ones. Why there are many resonances *missing* in the experimental spectrum is one of the most important problems in this field.

In fact, the experimentally established baryon spectrum is fully consistent with predictions from the di-quark model which assumes that two of the three quarks are bound, thus lowering the degrees of freedom in the harmonic oscillator parametrization [4]. The proponents of the symmetric quark model, however, argue that those resonant states have not been experimentally observed because those states do not couply strongly to πN, and almost all phase-shift analyses have been based on πN scattering, by far the most studied type of reactions.

Recently, a detailed study by Capstick and Roberts [5] on the decay of nucleon resonances into a strange baryon and a strange meson, suggests that some of the so called "missing" resonances couple strongly to $K\Lambda$ and $K\Sigma$. Since $K\Lambda$ photoproduction can only involve isospin 1/2 resonances, one expects that only a few of those states contribute to the s-channel for the reaction $\gamma p \to \mathrm{K}^+\Lambda$. Therefore, the analysis required to identify the contributing N^* resonances should be simpler than for other channels. The additional analysis of two isospin states of $\Sigma(1192)$ allows for a more complete understanding of associated strangeness production, and the search for "missing" Δ^* states. Capstick and Roberts predict that the signature of some missing resonances can be observed in these processes, and particularly the question of the $D_{13}(1960)$ resonance in Λ photoproduction will clearly be settled.

The $\gamma p \to \mathrm{K}^+\Lambda$ data from SAPHIR [7], published in 1998, shows an enhancement of the total cross section at a center-of-mass energy $W = \sqrt{s}$ of about 1.9 GeV. Mart and Bennhold [8] interpret this structure in the SAPHIR cross section as the contribution of the "missing" $D_{13}(1960)$ resonance. Saghai and collaborators [9] have shown that the SAPHIR data can as well be understood by taking into account the known resonances embodying off-shell effects for spin-3/2 resonances. Both groups point out that the presence of particular resonances in the s-channel have large effects on polarization observables. Besides the $D_{13}(1960)$ resonance, Capstick and Roberts predict sizeable contributions from other *missing* resonances at slightly higher W.

The use of polarized targets, together with polarized photon beams, and the measurement of the polarization of the recoiling hyperon will provide a complete set of measurements for the reactions $\gamma p \to K^+\Lambda$, $\gamma p \to K^+\Sigma^0$, and $\gamma p \to K^0\Sigma^+$. In combination with (i) data taken during the CLAS-g1 run period, using a beam of circularly polarized photons, and (ii) data taken during the CLAS-g8 run period, using a beam of linearly polarized photons, more than the required independent observables can be determined for all three reactions. Making use of algebraic correlations between various polarization observables will allow for consistency tests for all three data sets. The proposed measurements will facilitate an almost model-independent partial wave analysis (PWA) of these reactions to identify intermediate N^*, Δ^*, Λ^*, and Σ^* resonances. If any of those "missing resonances" are present in the measured energy spectrum and couple strongly to γp and KY, they will be identified since the corresponding multipoles provide clear signatures in most of the 14 (out of 16) single and double polarization observables we propose to measure.

These observables will be measured using the CLAS detector which is a unique magnetic spectrometer since it allows for the insertion of both longitudinally and transversely polarized targets while performing the simultaneous measurement of a set of obervables over a large angular range (except the very forward and backward directions). In addition, we make use of the high polarization of the CEBAF electron beam and the coherent beam facility in Hall B.

2 Motivation

2.1 Previous Measurements

The experimental study of the photoproduction of kaons started in the late 1950s, and was pursued until the early 1970s [10, 11, 12, 13]. The data extended from threshold up to 1.4 GeV.[3] Several sets of differential cross section data, a few total cross sections as well as hyperon polarization and polarized target measurements exist.

Twenty years later, new data for this reaction was obtained at the electron stretcher ring ELSA in Bonn using the SAPHIR detector [16]. SAPHIR acquired cross section and recoil polarization data for the reactions $\gamma p \to K^+\Lambda$ and $\gamma p \to K^+\Sigma^0$ from threshold up to 2 GeV photon energy [7, 17] and for the reaction $\gamma p \to K^0\Sigma^+$ up to $E_\gamma = 1.55$ GeV [18].

[3]Exceptions were cross section data at much higher photon energies: 4.0 GeV [14] and 20 GeV [15].

As shown in Fig. 1, the cross section for $\gamma p \to K^+\Lambda$ rises steeply from threshold up to its maximum at $W \approx 1.7$ GeV, and then decreases slowly. The SAPHIR data reveal a structure at about 1.9 GeV with a width of about 0.2 GeV superimposed on this general shape. The presence of this structure has been interpreted as experimental evidence for the excitation of a previously undiscovered baryon resonance.

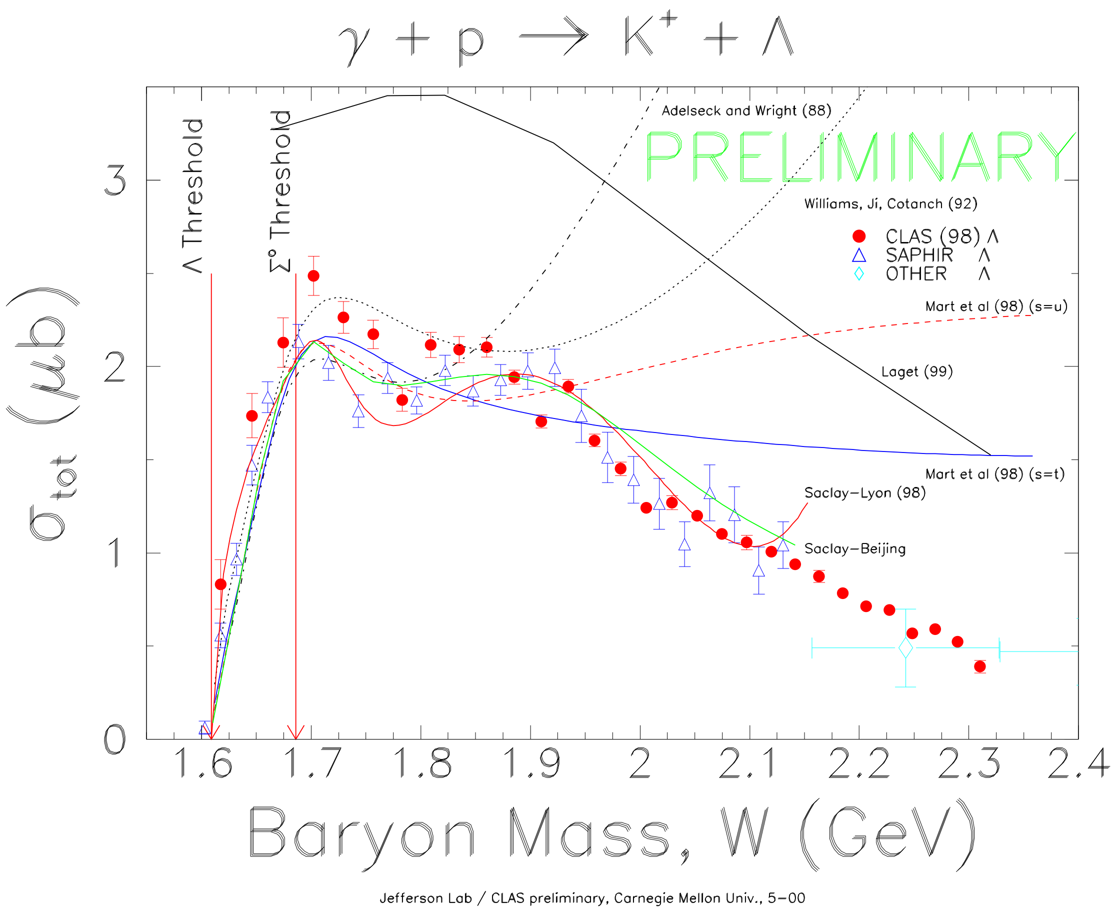

Figure 1: Preliminary cross section for $\gamma p \to K^+\Lambda$ from CLAS in comparison with various model predictions. The data was taken in 1998 (g1a run period).

A new data set obtained at Jefferson Laboratory using unpolarized and circularly polarized photon beams and the CLAS detector is currently being analyzed. The final results from this experiment (E-89-004 [19] as part of CLAS-g1) are expected to reveal any structure in the total cross section with improved accuracy. Preliminary results were presented at several workshops and conferences. Figure 1 shows the total cross section as a function of the c.m. energy W in comparison with several model predictions. The evolution of the $K^+\Lambda$ cross section confirms the general behavior of the SAPHIR results. Additionally, Fig. 1 indicates that the models have gradually improved in the description of the measured cross section.

In the case of polarization observables, existing data are sparse and fragmentary, and for most polarization observables there are no data at all. In fact, the current database for the reaction $\gamma p \to K^+\Lambda$ is not sufficient for a model independent analysis (PWA). The GW00 energy dependent solution of the SAID partial wave analysis was recently performed for $E_\gamma = 920 - 1600$ MeV [42], but it was found that the solution is not stable over a broad energy range because of the lack of data. The kinematic distribution of available data is given in Fig. 2.

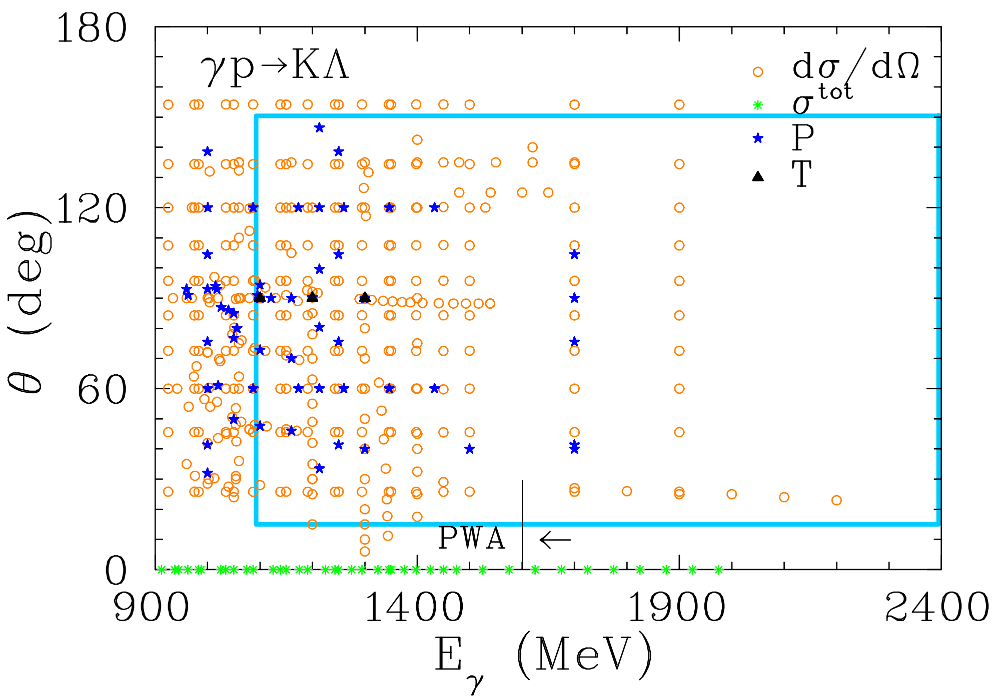

Figure 2: The current database of observables for the reaction $\gamma p \to K^+\Lambda$. The (light blue colored) box indicates the range of data points from the proposed experiment which will provide data for 7 polarization observables in the energy range $1.1 \leq E_\gamma \leq 2.5$ GeV for θ_{cm} between 15° and 150°, in addition to 4 observables ($d\sigma/d\Omega, P, C_x, C_z$) under analysis from CLAS-g1 and 3 observables (Σ, O_x, O_z) to be extracted from CLAS-g8 data.

The following data points are available for the reaction $\gamma p \to K^+\Lambda$:

Observable:	E_γ=0.92–1.6 GeV,	E_γ=1.6–2.4 GeV
differential cross section ($d\sigma/d\Omega$):	323 data points,	30 data points
total cross section (σ^{tot}):	32	8
recoil polarization (P):	53	6
target polarization (T):	3	0

There are no published data for the beam asymmetry Σ nor for any double polarization observable.

There are less experimental results published on Σ photoproduction.
For the reaction $\gamma p \to K^+\Sigma^0$ the following data are available:

Observable:	E_γ=1.05–1.6 GeV,	E_γ=1.6–2.4 GeV
differential cross section ($d\sigma/d\Omega$):	210 data points,	36 data points
total cross section (σ^{tot}):	34	10
recoil polarization (P):	9	1

Because of its low cross section only a few experimental results are available for $\gamma p \to K^0\Sigma^+$:

Observable:	E_γ=1.05–1.6 GeV,	E_γ=1.6–2.4 GeV
differential cross section ($d\sigma/d\Omega$):	18 data points,	0 data points
total cross section (σ^{tot}):	5	0

2.2 Theoretical Formalism

The theoretical description of the associated production of strange particles has been pursued for more than four decades, but the underlying reaction mechanism is still not well understood. This might be attributed to the complex role played by the *strange* quark. This new degree-of-freedom – in addition to those of *up* and *down* quark – can result in the excitation of several nucleon and hyperon resonances that are not present in pion photoproduction.

The phenomenological description of kaon photoproduction has been based on dynamical models using hadronic degrees of freedom. Most of the analyses have been done at the tree level, providing a simple tool to parametrize the reaction by some unkown coupling constants which are adjusted to reproduce the experimental data.

In a tree-level isobar model, the Feynman diagrams contributing to $K^+\Lambda$ photoproduction are shown in Fig. 3, diagrams (a) to (g). Diagrams (a) through (d) constitute the Born terms and diagrams (e) through (g) constitute resonant terms in the t–, u–, and s–channel, respectively. For $K\Sigma$ photoproduction, there are additional contributions from Δ and Δ^* states, shown as additional graph in Fig. 3, diagram (h).

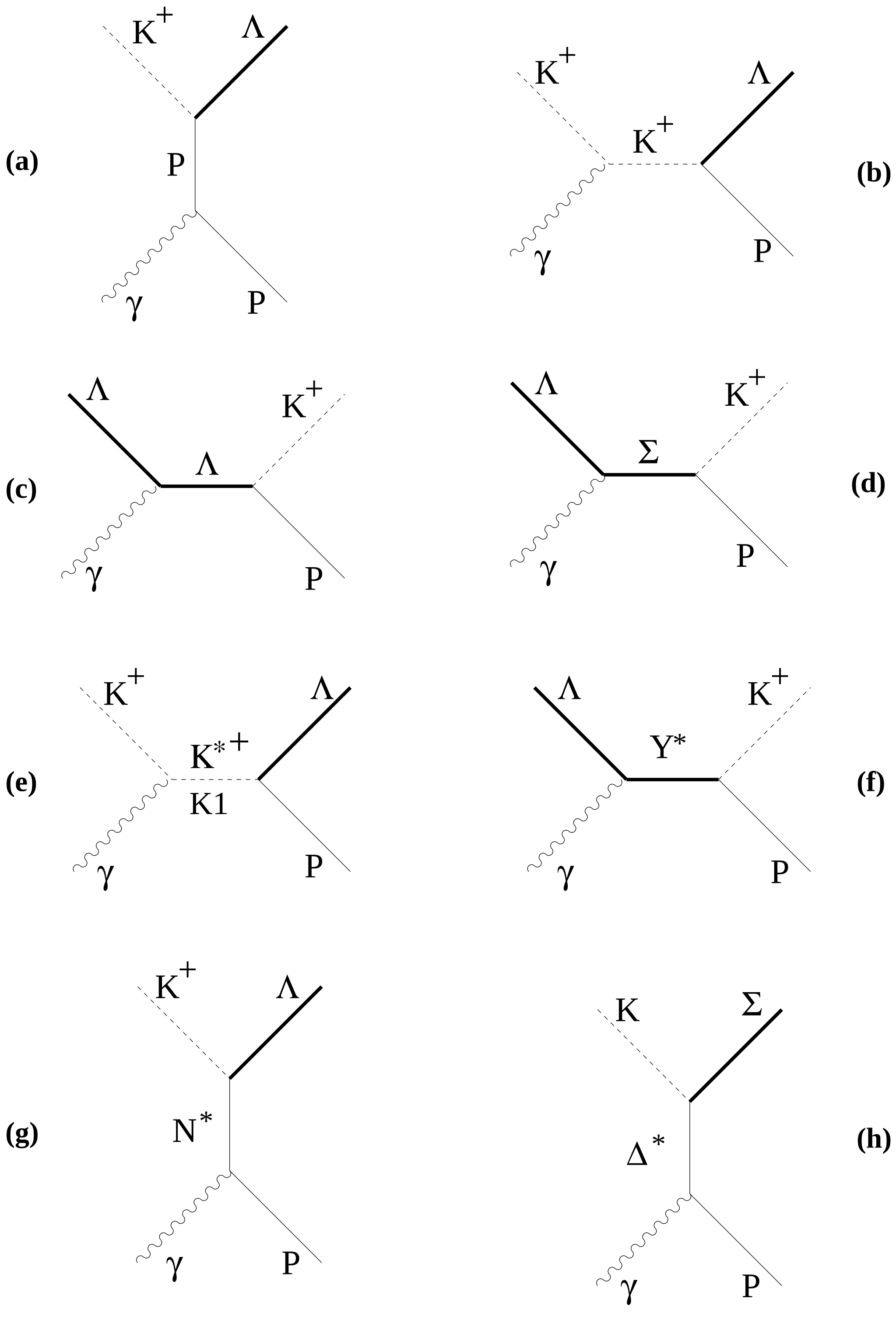

Figure 3: Feynman diagrams for the process $\gamma p \to K^+\Lambda$ (diagrams (a) to (g); similar for $\gamma p \to K\Sigma$, except the additional graphs involving Δ^*–exchanges (h).

The coordinate systems and kinematical variables used in the description of these reactions in the center-of-mass reference frame are defined in Fig. 4.

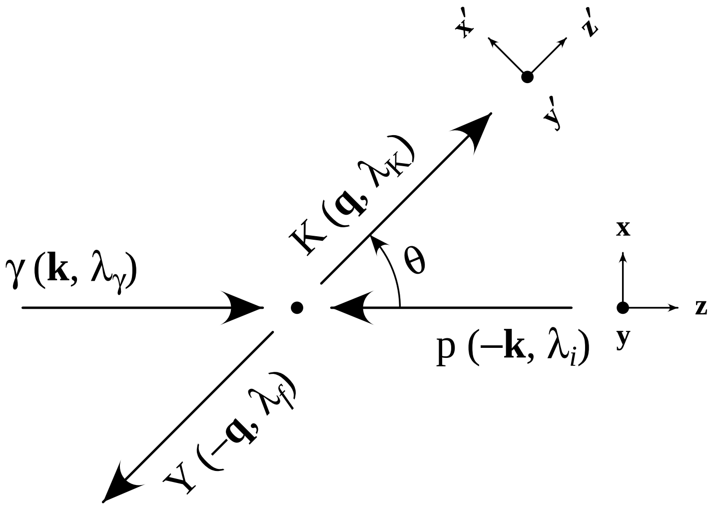

Figure 4: Coordinate systems and kinematical variables for Kaon photoproduction.

The differential cross section has the form

$$\frac{d\sigma}{d\Omega_{cm}} = \frac{(E_p + M_p)(E_Y + M_Y)}{128\pi^2 s} \frac{|\,\mathbf{q}\,|}{|\,\mathbf{k}\,|} Tr(\mathcal{F}\mathcal{F}^\dagger) \ , \tag{1}$$

where $\mathbf{k}$ is the incoming photon momentum, $\mathbf{q}$ is the outgoing Kaon momentum in the center-of-mass frame, and $\mathcal{F}$ is defined as

$$\mathcal{F} = f_1 \boldsymbol{\sigma} \cdot \boldsymbol{\epsilon} + i f_2 \frac{(\boldsymbol{\sigma} \cdot \boldsymbol{q})(\boldsymbol{\sigma} \cdot \ \boldsymbol{k} \times \boldsymbol{\epsilon})}{|\,\mathbf{q}\,||\,\mathbf{k}\,|} + f_3 \frac{(\boldsymbol{\sigma} \cdot \boldsymbol{k})(\boldsymbol{q} \cdot \boldsymbol{\epsilon})}{|\,\mathbf{q}\,||\,\mathbf{k}\,|} + f_4 \frac{(\boldsymbol{\sigma} \cdot \boldsymbol{q})(\boldsymbol{q} \cdot \boldsymbol{\epsilon})}{\mathbf{q}^2} \ , \tag{2}$$

where the f_i are the Chew, Goldberger, Low, and Nambu (CGLN) amplitudes [20], and ϵ is the polarization vector of the photon.

The set of experiments that completely describes the photoproduction of Λ and Σ consists of measurements using unpolarized beam, circularly and linearly polarized beam, unpolarized target, longitudinally and transversely polarized target. If one also measures the polarization vector of the recoiling hyperon, a total of 16 single and double polarization observables can be obtained.[4] These observables produce redundant information which is reflected by nonlinear relations among them. For example, the expressions

$$T_x^2 + T_z^2 + L_x^2 + L_z^2 = 1 + \Sigma^2 - P^2 - T^2 \ , \tag{3}$$

$$T_x L_z - T_z L_x = \Sigma - PT \ , \tag{4}$$

[4]The expressions of all single and double polarization observables and their algebraic relations are listed in Appendix A.

relate the observables obtained in an experiment on transversely polarized target (T, T_x, T_z) with the observables L_x and L_z which are measured on longitudinally polarized target. Kaon photoproduction is described by four complex CGLN amplitudes but, in order to resolve ambiguities in the relative phases between the amplitudes, at least 8 independent measurements have to be performed [21]. A complete set of independent observables requires the measurement of polarization observables involving a polarized target. We want to point out that 8 measurements are only sufficient in case of negligible statistical and systematical errors.

2.3 Theoretical Predictions

In the range of photon energies available at Jefferson Lab, the electromagnetic production of kaons is expected to result in part from the excitation of non-strange baryons in the s-channel, which subsequently decay into a strange baryon and a strange meson [5]. The constituent quark model of Capstick and Roberts [3] predicts many excited baryon states in this energy range that have not been seen in πN elastic and inelastic scattering; however, only a few of them have a significant $K\Lambda$ or $K\Sigma$ branching ratio. In Table 1 the photoproduction amplitudes and the decay amplitudes into the $K\Lambda$ and $K\Sigma$ channels for several nucleon states, as predicted by Capstick and Roberts, are listed. Only those resonances are displayed that have significant photon– as well as $K\Lambda$ and/or $K\Sigma$ coupling based on the strength of the product

$$\chi_\lambda = \Gamma_{KY}^{1/2} A_\lambda / \Gamma_0 \ ,$$

where A_λ is the electromagnetic excitation amplitude $\gamma N \rightarrow N^*$ for helicity λ, Γ_0 and Γ_{KY} are the total and the KY decay widths of a given N^* (Y denotes Λ, Σ^0, or Σ^+). From these predictions it is expected that the state $N\frac{3}{2}^-(1960)[D_{13}]_3$ will be clearly identified, and significant contributions from the other states will be observed in the reactions $\gamma p \rightarrow \mathrm{K}^+\Lambda$, $\gamma p \rightarrow \mathrm{K}^+\Sigma^0$, and $\gamma p \rightarrow \mathrm{K}^0\Sigma^+$.

The predictions of other quark models will be taken under consideration as well, especially the large N_c model for which the calculations of the 70^- baryon spectrum have recently been published [6]. The N^* and Δ^* resonances ($W \leq 1.72$ GeV) of this multiplet are well established; as soon as predictions for higher mass states are calculated we will incorporate those into our considerations.

Model state	Nπ state	$A_{\frac{1}{2}}$	$A_{\frac{3}{2}}$	$A_{K\Lambda}$	$A_{K\Sigma}$
$N^-_{\frac{1}{2}}(1945)[S_{11}]_3$	$N(2090)^*$	12		2.3±2.7	$2.1^{+1.3}_{-1.4}$
$N^-_{\frac{3}{2}}(1960)[D_{13}]_3$	$N(2080)^{**}$(?)	36	-43	$-5.6^{+1.7}_{-1.3}$	-0.7±0.3
$N^-_{\frac{3}{2}}(2055)[D_{13}]_4$	$N(2080)^{**}$(?)	16	0	$-2.7^{+0.9}_{-0.8}$	$1.8^{+0.7}_{-0.8}$
$N^-_{\frac{5}{2}}(2080)[D_{15}]_2$		-3	-14	$-2.9^{+0.8}_{-0.4}$	$-2.4^{+0.9}_{-0.5}$
$N^-_{\frac{7}{2}}(2090)[G_{17}]_1$	$N(2190)^{****}$	-34	-28	$-1.3^{+0.4}_{-0.6}$	-0.2±0.1
$N^-_{\frac{5}{2}}(2095)[D_{15}]_3$	$N(2200)^{**}$	-2	-6	$-1.7^{+0.5}_{-0.4}$	$2.5^{+0.6}_{-0.9}$
$N^+_{\frac{9}{2}}(2345)[H_{19}]_1$	$N(2250)^{****}$	-29	13	-0.4±0.1	1.1±0.3
$\Delta^-_{\frac{1}{2}}(2035)[S_{31}]_2$	$\Delta(1900)^{***}$	20			-1.9±0.3
$\Delta^-_{\frac{3}{2}}(2080)[D_{33}]_2$	$\Delta(1940)^*$	-20	-6		1.1±0.7
$\Delta^-_{\frac{1}{2}}(2140)[S_{31}]_3$	$\Delta(2150)^*$	4			-4.1±2.4
$\Delta^-_{\frac{5}{2}}(2155)[D_{35}]_1$	$\Delta(1930)^{***}$	11	19		2.1±0.4
$\Delta^-_{\frac{9}{2}}(2295)[H_{39}]_1$	$\Delta(2400)^{**}$	-14	-17		$1.4^{+1.0}_{-0.8}$
$\Delta^+_{\frac{7}{2}}(2370)[F_{37}]_2$	$\Delta(2390)^*$	-33	-42		$1.9^{+0.4}_{-0.5}$

Table 1: Photoproduction amplitudes and decay amplitudes into the $K\Lambda$ and $K\Sigma$ channels for some negative-parity excited nucleon states according to the constituent quark model of Capstick and Roberts. Amplitudes are in units of 10^{-3} GeV$^{-\frac{1}{2}}$. Data taken from references [3] and [5].

Most phenomenological descriptions of the reactions $\gamma p \to K\Lambda$ and $\gamma p \to K\Sigma$ below $E_\gamma \approx 2.5$ GeV are based on the isobar model [24, 25, 26, 27, 28, 29]. These models use an effective Lagrangian approach in which a number of tree diagrams are evaluated with coupling constants partly fixed from hadronic and electromagnetic data.

Since the publication of the comparatively high quality data from SAPHIR, the efforts in the theoretical description of kaon photoproduction have been intensified. A coupled-channel calculation that includes final-state interactions has linked the photoproduction process $p(\gamma, K^+)\Lambda$ to the hadronic process $p(\pi^-, K^0)\Lambda$ [30]. In principle, this unitary coupled-channels framework allows for separating background from resonance contributions, but a much larger set of experimental data points, especially for $K\Lambda$ photoproduction, is required to resolve ambiguities. In a different approach, the coupled-channels model for pion production [31], incorporating off-shell and final-state interactions, is being extended to KY channels. A first study [32] reveals that coupled-channel effects from $\pi^0 p$ and $\pi^+ n$ intermediate states contribute significantly to $K\Lambda$ photoproduction.

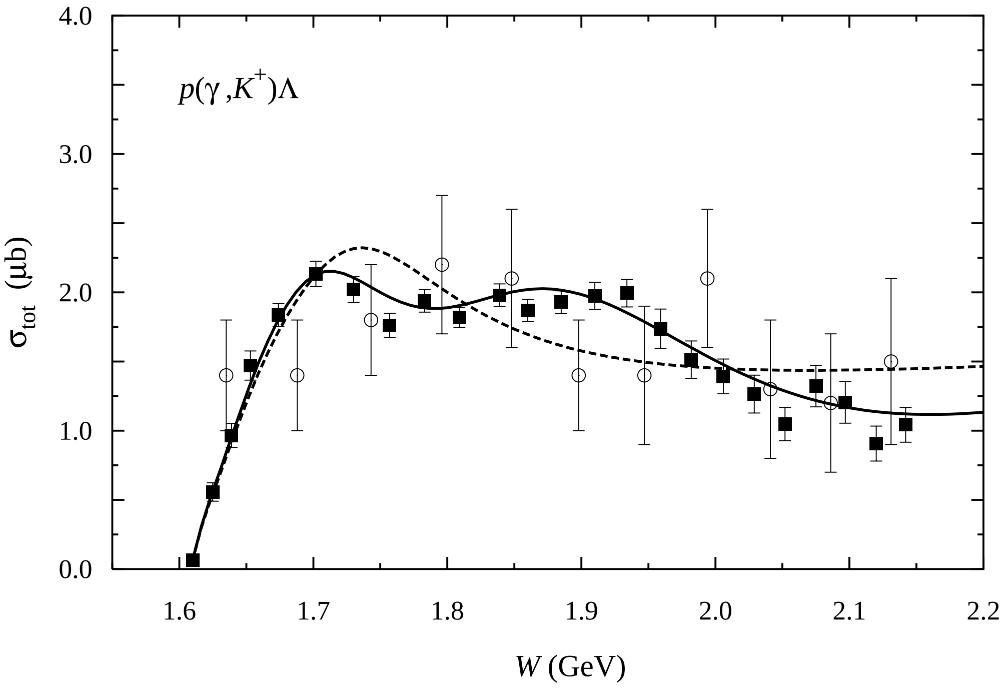

Figure 5: Total cross section for $K\Lambda$ photoproduction on the proton. The solid line is obtained from the Mart–Bennhold model including the $D_{13}(1960)$ resonance, while the dashed line shows the calculation without the $D_{13}(1960)$ state. The SAPHIR data [7] are denoted by solid squares, previous data by open circles. Taken from Ref. [8].

Over the last two years, the theoretical interpretation of the recent SAPHIR data triggered a lively discussion about the discovery of a missing baryon resonance. A calculation by Mart and Bennhold [8] based on the tree-level isobar model of Ref. [33], claims that, in order to describe the structure around $W \approx 1.9$ GeV in the $p(\gamma, K^+)\Lambda$ data from SAPHIR, it is necessary to include the $D_{13}(1960)$ resonance predicted by the quark model. Hints for the existence of this resonance were already found in two separate analyses of $p(\pi^-, K^0)\Lambda$ data [34, 35]. In Fig. 5, the results of the calculation with and without the contribution of the $D_{13}(1960)$ state are compared with the SAPHIR data. Figure 6 shows the predictions for the target asymmetry T with and without contributions of the $D_{13}(1960)$ state. The calculations show that T provides a high sensitivity for the inclusion of this resonance for photon energies above 1.2 GeV.

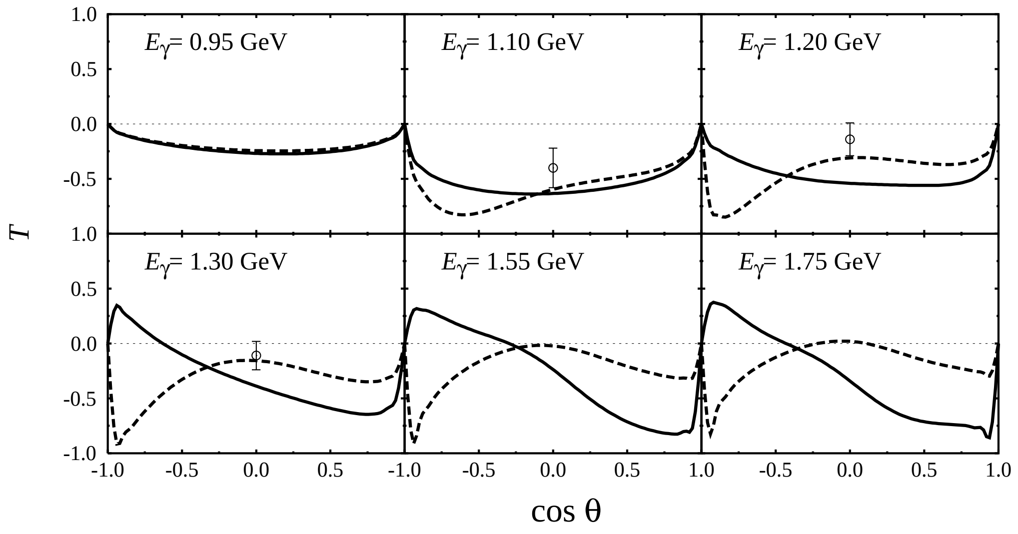

Figure 6: Target asymmetry T for $\gamma p \to K^+\Lambda$. The solid line is obtained from the Mart–Bennhold model [8] including the $D_{13}(1960)$ state, while the dashed line shows prediction without the $D_{13}(1960)$ resonance. Experimental data from [12].

According to Bennhold and Mart, the evidence for the existence of the $D_{13}(1960)$ resonance has been strengthened by the analysis of the kaon electroproduction data from Hall C at Jefferson Lab [36]. An extension of their isobar model to finite Q^2 shows that the data cannot be explained without the presence of the $D_{13}(1960)$ [37].

Contrary to the conclusions of Bennhold and Mart, Saghai *et al.* [9, 38, 39] have pointed out that a fit to the existing $K\Lambda$ photoproduction data does not require a missing $D_{13}(1960)$ resonance in the s-channel. In Fig. 7 the Mart–Bennhold fit (*dot-dashed* curve) to total cross section data from SAPHIR is compared to various fits which do not include the $D_{13}(1960)$ resonance. The Saclay–Lyon model [27], which contains the same nucleon resonances ($S_{11}(1650), P_{11}(1710), P_{13}(1720)$) as the Mart–Bennhold model except the $D_{13}(1960)$ shows a monotonic decrease above $W \approx 1.73$ GeV (*dashed* curve). The incorporation of off-shell effects (*dotted* curve) causes an almost flat behavior at W between 1.8–1.9 GeV. If additionally two Λ^* states are included ($P_{01}(1810), P_{03}(1890)$), the experimental cross section data as well as existing recoil polarization and electroproduction data are well reproduced (*full* curve). The *bold faced dashed* curve shows the result of a calculation in the framework of the constituent quark model approach [39, 40] which reproduces the existing experimental data as well.

One conclusion of these studies is that measurements of further polarization observables will be necessary to elucidate the contribution of various N^* resonances to this channel, including

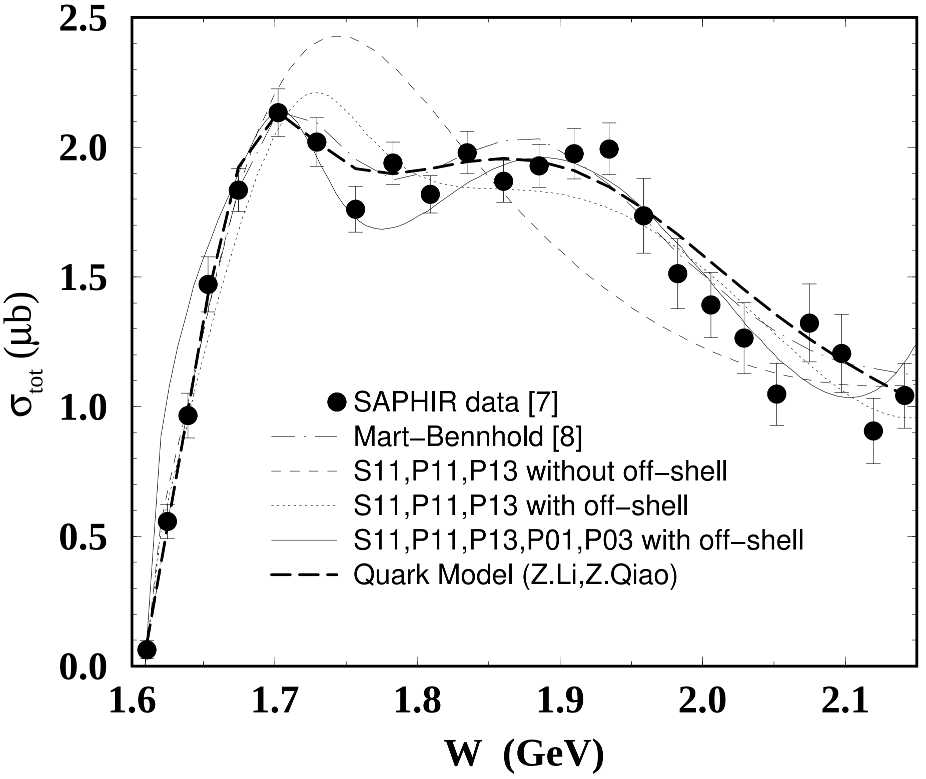

Figure 7: Fit results for the total cross section of $\gamma p \rightarrow K^+\Lambda$. The dot-dashed line shows the prediction of the Mart–Bennhold model which includes the "missing" $D_{13}(1960)$ resonance; the other curves represent fits without contributions of the $D_{13}(1960)$: the dashed, dotted, and full curves show stages of the fits to the improved Saclay–Lyon model (dashed curve) which include off-shell effects (dotted curve) and Λ^* exchange (full curve). The dashed bold faced curve represents result from quark model calculations.

resonances that may yet be undiscovered.

Variations of parameters in the Kaon-MAID pole fit confirm this observation. High sensitivity to the coupling of the $D_{13}(1960)$ resonance is found in the double polarization observables F, G, H, which combine beam and target polarization, and L_x. Figure 8 shows the Kaon-MAID result for the double polarization observable L_x which involves a longitudinally polarized target and the in-plane (x') component of the recoil polarization. The solid line shows the full calculation including $D_{13}(1960)$, whereas the dashed curve displays the result for the case that the D_{13} contribution is turned off.[5]

[5] Kaon-MAID represents the model of Mart and Bennhold. The calculations in Kaon-MAID are based on fits *including* $D_{13}(1960)$, therefore turning off the D_{13} is not fully comparable with a best fit without this resonance.

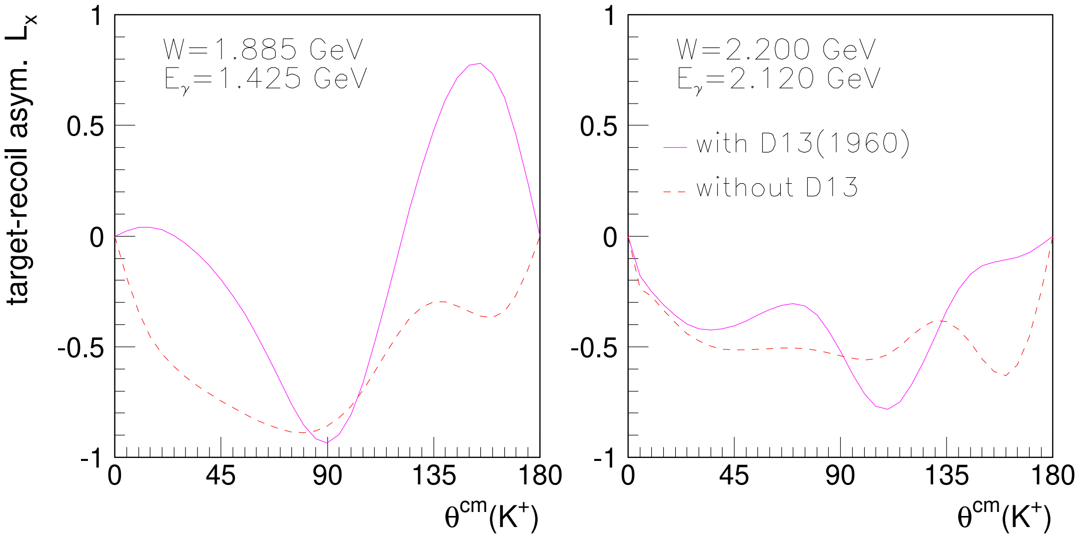

Figure 8: Target-Recoil polarization L_x for $\gamma p \to K^+\Lambda$ at different photon energies. The solid (purple) line shows the full Kaon-Maid fit result including the $D_{13}(1960)$ state; the dashed (red) line shows the result without this resonance.

Experimental data using a polarized target and polarized photon beams up to E_γ=2.5 GeV will enable us to search not only for additional higher resonant states as predicted by the constituent quark model (cf. Table 1), but also to investigate the transition between low– and high–energy hyperon production. The partial wave analysis of $\gamma p \to K^+\Lambda$ up to photon energies above 2 GeV [42] may bridge the gap between the low- and high-energy regions as was shown for pion photoproduction [43] and NN elastic scattering [44].

The general shape of the $K\Lambda$ photoproduction cross section above 2 GeV appears to be consistent with a high–energy behavior suggested by the Regge trajectory exchange model of J.M. Laget and M. Guidal [45] which describes the 4 GeV data of Anderson [14], and predicts an energy dependence of s^{-3} at $\theta_{cm}(K^+) = 90°$. The predicted differential cross section is shown in Fig. 9 for one energy setting (E_γ = 2.7 GeV). Nevertheless, this model cannot describe interference phenomena via polarization observables.

The s-channel contributions in $K\Sigma$ photoproduction can be studied in a similar way since these data will be collected simultaneously. Since the Σ is a SU(2) isovector state, it is not sufficient to focus on a single $K\Sigma$ channel, e.g. the reaction $\gamma p \to K^+\Sigma^0$, which – in a phenomenological description – can be treated in the same way as $\gamma p \to K^+\Lambda$ except for the occurrence of additional Δ, Δ^*

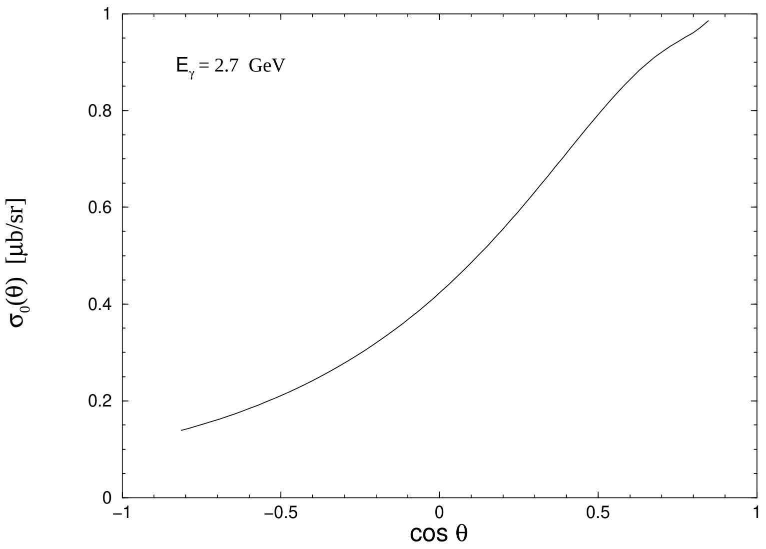

Figure 9: Regge model prediction for the differential cross section of $\gamma p \to K^+\Lambda$ at $E_\gamma = 2.7$ GeV. Calculation based on [45].

resonance contributions (cf. Fig. 3, diagram (h)). A consistent description of Σ photoproduction has to include the charged Σ channels in order to determine the various coupling parameters in Σ photoproduction.[6]

2.4 Partial Wave Analysis

With the measurement of almost all single and double polarization observables over a large energy range, an accurate description of associated strangeness production will be achieved, and this will facilitate a partial wave analysis of the resulting data in order to identify the contributing resonances. The partial wave analyses of $K^+\Lambda$, $K^+\Sigma^0$, and $K^0\Sigma^+$ photoproduction require improved data for all energies in order to increase the constraints for the PWA, and to extend the analysis to higher energies. Polarization observables are particularly important for distinguishing resonance contributions from other (non-resonant) production dynamics; the availability of accurate polarization data, as proposed by this experiment, will allow for disentangling any significant multipole contributions. Although it is sufficient to perform eight independent measurements to extract the

[6]This experiment aims to measure Σ^0 and Σ^+ production on a proton target. A corresponding experiment on a polarized deuteron target to measure the remaining 2 Σ photoproduction channels ($\gamma n \to K^0\Sigma^0$, $\gamma n \to K^+\Sigma^-$) will be subject to a future proposal.

CGLN or helicity amplitudes, the multipole decomposition needs additional information to determine the relative phases of the individual multipoles. We will employ complementary methods in order to extract these quantities: (a) an energy independent likelihood analysis to be performed for each energy bin; (b) an energy dependent partial wave analysis which was recently developed by the SAID group and is based on their successful PWA for pion production.

Likelihood analyses are often employed in partial wave analysis techniques used in hadron spectroscopy to extract information about spin, parity, isospin, and decay properties of hadronic resonances. Energy independent likelihood analyses have been used extensively to study meson spectra [46]. We are going utilize the tools developed for meson spectroscopy which will provide additional and complementary techniques for our study of baryon resonances. We refer the reader to Appendix C for further details.[7]

The SAID partial wave analysis is performed by expanding each of the helicity amplitudes in terms of multipoles which depend on energy. The amplitudes are varied in a χ^2 fitting procedure to give a best fit to all measured observables. Since experimental data only exist for the differential cross section and Λ recoil polarization, thus are not sufficiently complete for a fit to the data, the fit is constrained to low partial waves. Sufficient data for additional observables will easily guide or correct the fit parameters, and will allow for reducing these constraints.

We compared the energy dependent solution of the SAID PWA for the $K\Lambda$ channel which does not require any resonant D-wave strength at $E_\gamma \approx 1.4 - 1.5$ GeV with predictions of the model of B. Saghai [9] which includes off-shell effects – but no $D_{13}(1960)$ – and of the Mart-Bennhold model [8] which includes the $D_{13}(1960)$ resonance. In Figs. 10 – 13 all sixteen single and double polarization observables for the reaction $\gamma p \to \mathrm{K}^+\Lambda$ at $E_\gamma = 1.5$ GeV are plotted as functions of the K^+ production angle $\theta_{cm}(K^+)$. The solution of the SAID partial wave analysis (GW00) is shown as *solid* curves, the predictions of the Saghai model as *dotted* curves, and the predictions of the Mart–Bennhold model as *dashed* curves. The fit results of both models do not take into account the systematic uncertainties of the experimental data, whereas the SAID PWA allows for varying the normalization of each of the data sets (within in sytstematic errors quoted by the experiments).

The plots show strong variations of all polarization observables as function of the K^+ production angle. For almost all polarization observables, the results of the model predictions differ significantly from the SAID solution.

[7] Even if this method won't reach the required sensitivity to reliably extract the contributing partial waves in a given energy bin, it provides a powerful means for detailed checks of the Monte Carlo description of the detector acceptance.

The same comparison has been made for the Σ channels $\gamma p \to \mathrm{K}^+\Sigma^0$ and $\gamma p \to \mathrm{K}^0\Sigma^+$. Figures 14 and 15 show the solutions for the differential cross section and some polarization observables which involve a polarized target. Like in the $\mathrm{K}^+\Lambda$ case, the differential cross section for $\mathrm{K}^+\Sigma^0$ photoproduction has been measured – the difference between the Mart-Bennhold model and the SAID solutions is therefore comparatively small, whereas predictions for single and double polarization observables differ strongly. In fact, all polarization observables which involve a polarized target and/or a linearly polarized beam show the largest variations. This is also the case for $\mathrm{K}^0\Sigma^+$ photoproduction where even cross section data hardly exist.

In combination with the KY photoproduction experiments which are part of the CLAS-g1 and CLAS-g8 run periods, the proposed experiment will measure the following 14 observables with high accuracy: $\mathbf{d\sigma/d\Omega, P, \Sigma, T, E, H, T_x, T_z, L_x, L_z, C_x, C_z, O_x}$, and $\mathbf{O_z}$. Error bars on the *zero line* provide the expected statistical uncertainties from the CLAS photon experiments for the extracted observables in this energy bin ($W = 1.905 - 1.930$ GeV). The expected errors are shown for 10 angular bins (between 15^o and 165^o) except for $\mathrm{K}^0\Sigma^+$ production which suffers from low cross section and more sophisticated data analysis. The estimated systematic uncertainties are discussed in Sec. 4.4.

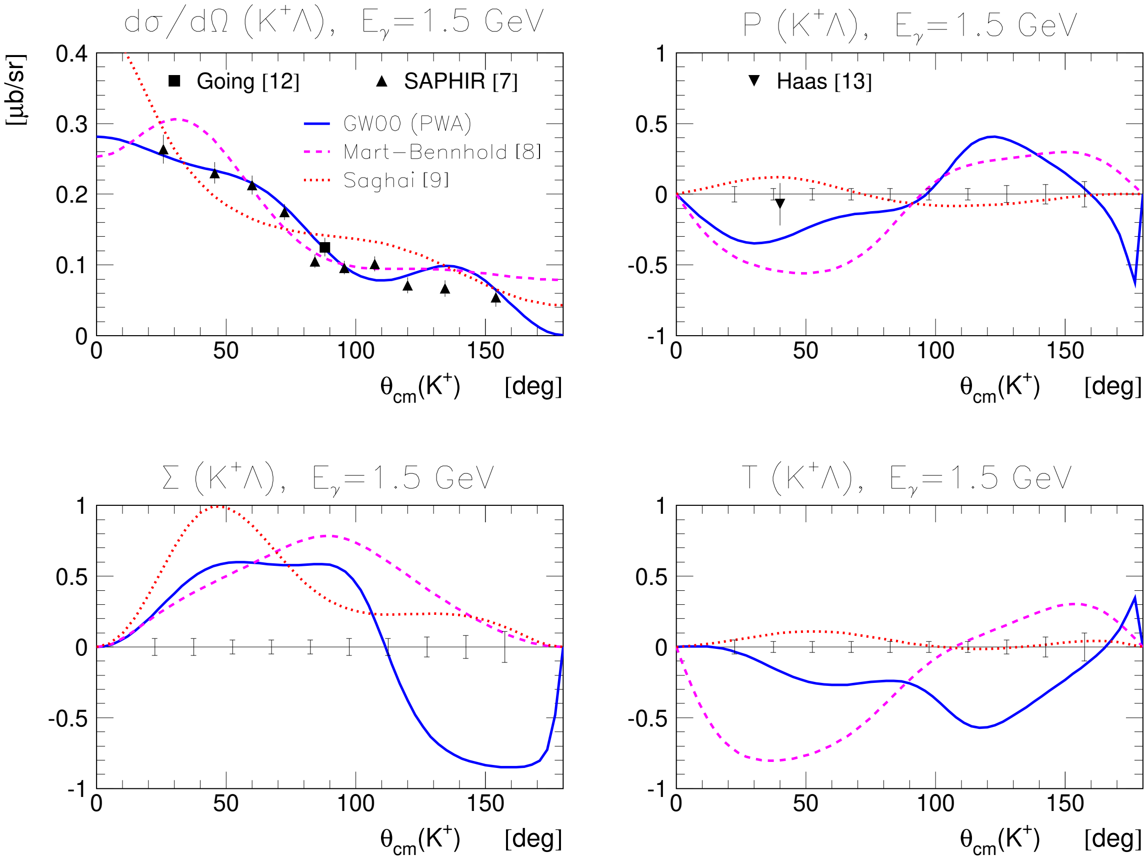

Figure 10: **Single polarization observables** for the reaction $\gamma p \to \mathrm{K}^+\Lambda$ at $E_\gamma = 1.5$ GeV:
DSG: differential cross section, **P**: Λ recoil polarization, **Σ**: beam asymmetry, **T**: target asymmetry. The *solid curves* represent the SAID PWA solution (GW00), the *dotted curves* the results of Saghai's model [9], and the *dashed curves* the results of the Mart–Bennhold model [8]; the latter includes a resonant D-wave ($D_{13}(1960)$) at this energy, the others not. The *error bars on the zero line* show the expected errors from this experiment together with CLAS-g1 and CLAS-g8.

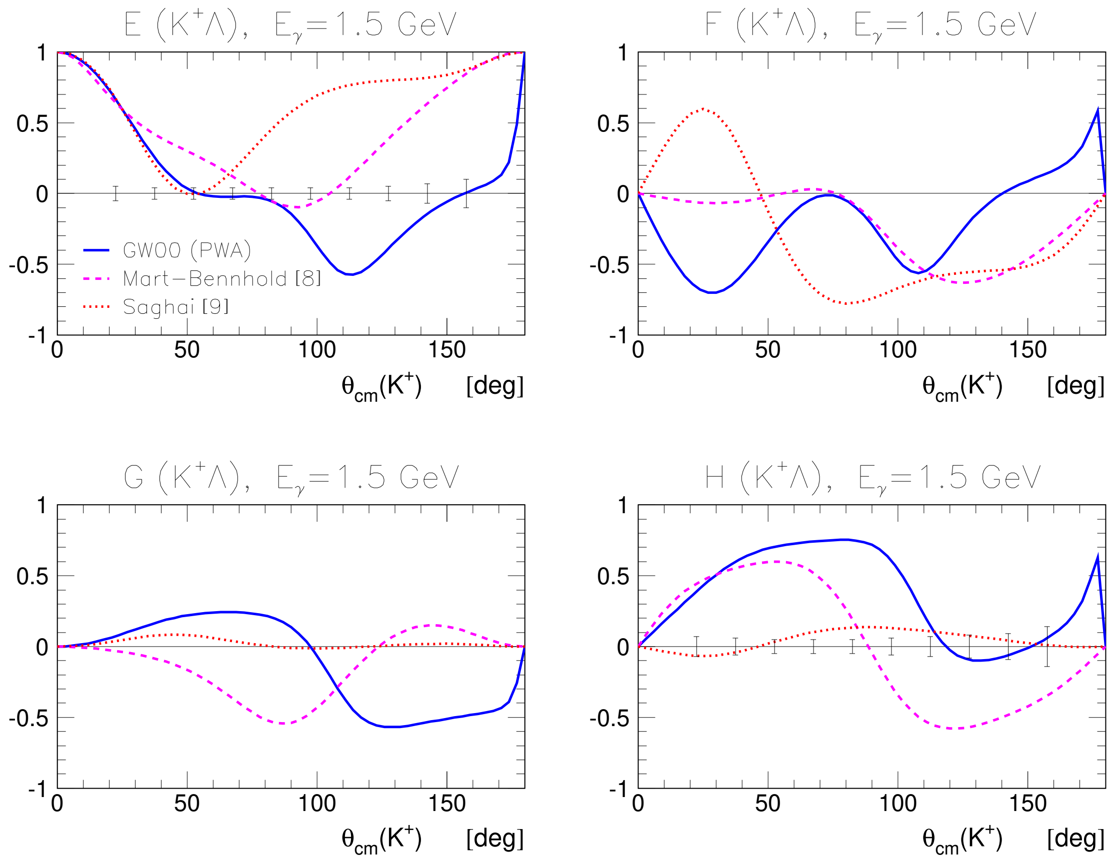

Figure 11: Predictions for the **beam-target polarization observables** for the reaction $\gamma p \rightarrow K^+\Lambda$. The *solid curves* represent the SAID PWA solution (GW00), the *dotted curves* the results of Saghai's model [9], and the *dashed curves* the results of the Mart–Bennhold model [8]; the latter includes a resonant D-wave ($D_{13}(1960)$) at this energy, the others not. The *error bars on the zero line* show the expected errors from this experiment.

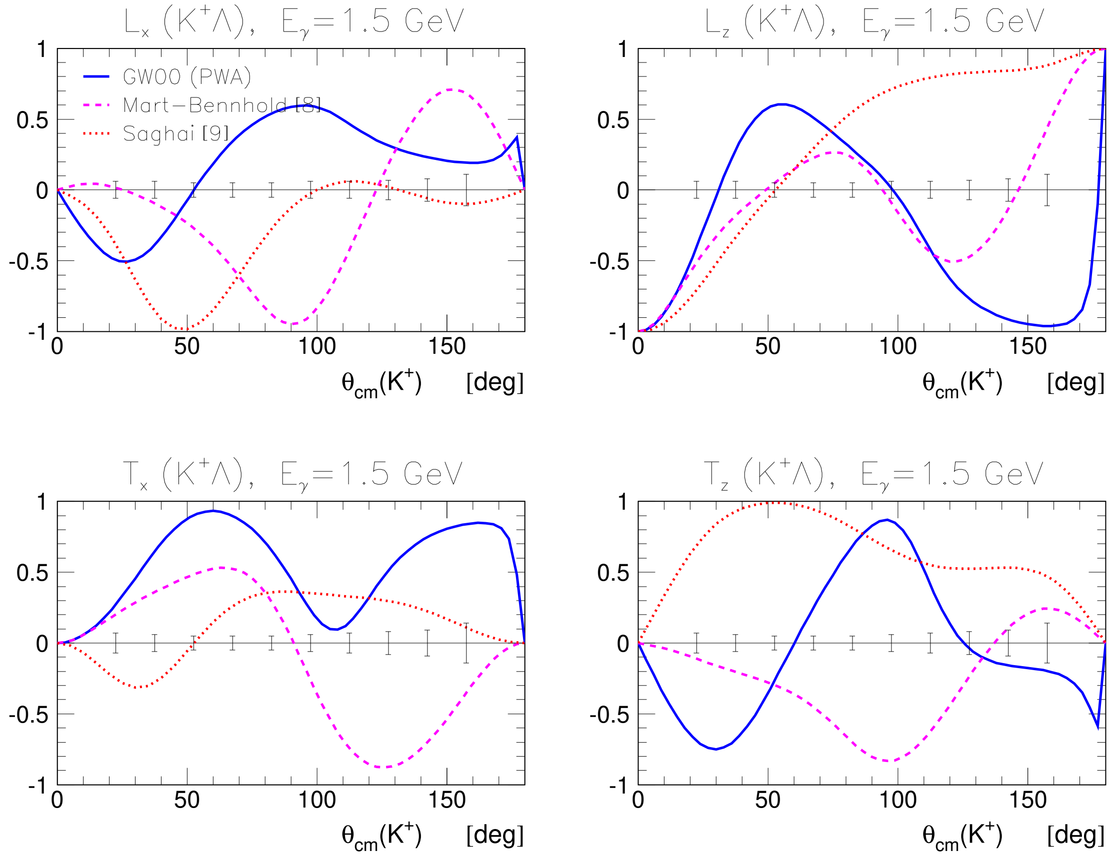

Figure 12: Predictions for the **target-recoil polarization observables** for the reaction $\gamma p \rightarrow \mathrm{K}^+\Lambda$. The *solid curves* represent the SAID PWA solution (GW00), the *dotted curves* the results of Saghai's model [9], and the *dashed curves* the results of the Mart–Bennhold model [8]; the latter includes a resonant D-wave ($D_{13}(1960)$) at this energy, the others not. The *error bars on the zero line* show the expected errors from this experiment.

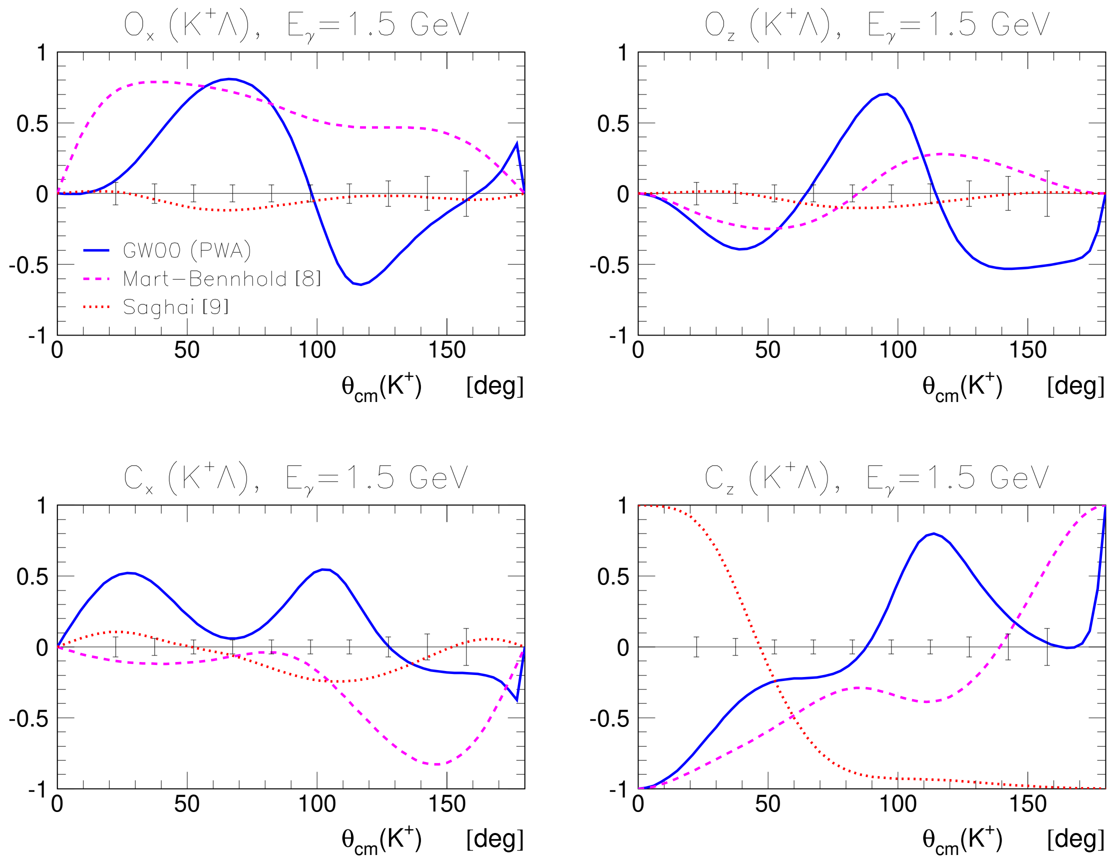

Figure 13: Predictions for the **beam-recoil polarization observables** for the reaction $\gamma p \rightarrow K^+\Lambda$. The *solid curves* represent the SAID PWA solution (GW00), the *dotted curves* the results of Saghai's model [9], and the *dashed curves* the results of the Mart–Bennhold model [8]; the latter includes a resonant D-wave ($D_{13}(1960)$) at this energy, the others not. The *error bars on the zero line* show the expected errors from this experiment together with CLAS-g1 and CLAS-g8.

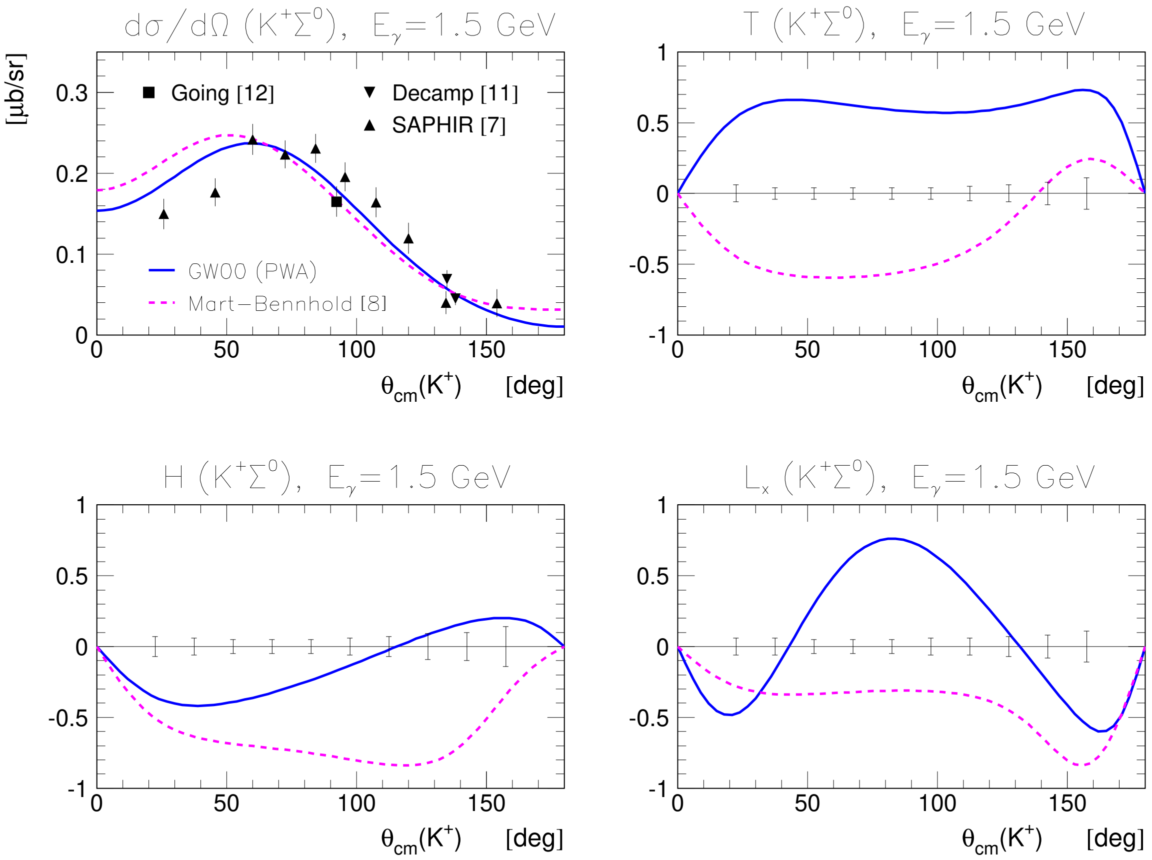

Figure 14: Predictions for cross section and some polarization observables for $\gamma p \rightarrow K^+\Sigma^0$:
DSG: differential cross section, **T**: target asymmetry, **H**: lin. beam–transv. target polarization, **Lx**: long. target–recoil polarzation. The *solid* curves represent the SAID PWA solution (GW00) and the *dashed* curves the results of the Mart–Bennhold model [8]. The *error bars on the zero line* show the expected errors from this experiment.

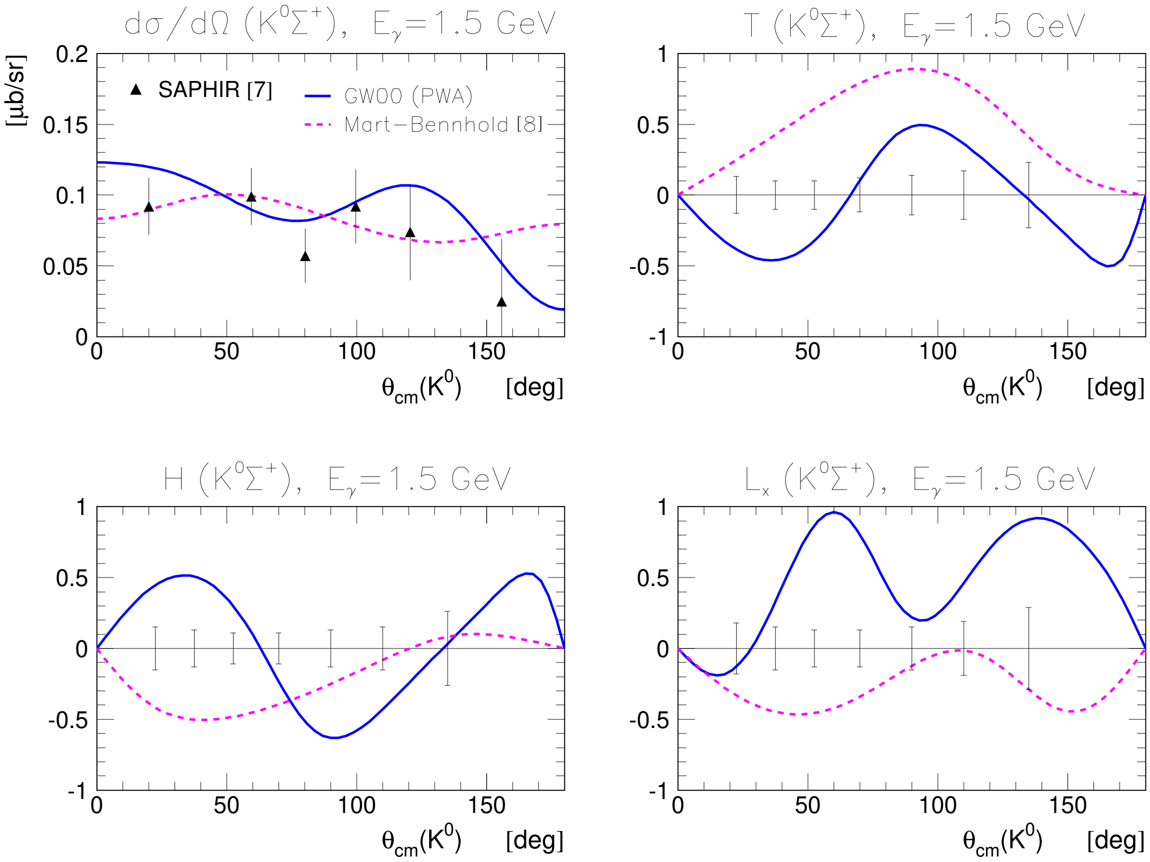

Figure 15: Predictions for cross section and some polarization observables for $\gamma p \to \mathrm{K}^0\Sigma^+$:
DSG: differential cross section, **T**: target asymmetry, **H**: lin. beam–transv. target polarization, **Lx**: long. target–recoil polarzation. The *solid* curves represent the SAID PWA solution (GW00) and the *dotted* curves the results of the Mart–Bennhold model [8]. The *error bars on the zero line* show the expected errors from this experiment.

3 Acceptance Studies

3.1 Acceptance for $\gamma p \rightarrow K^+\Lambda$ and $\gamma p \rightarrow K^+\Sigma^0$ with CLAS

The acceptance of the CLAS detector for this reaction is performed by means of the GEANT based simulation program for CLAS and the CLAS event reconstruction program. After a few tests with larger targets we set the length of the target to 25 mm and its radius to 7 mm in order to reduce energy loss and multiple scattering in C_4H_9OH (butanol).

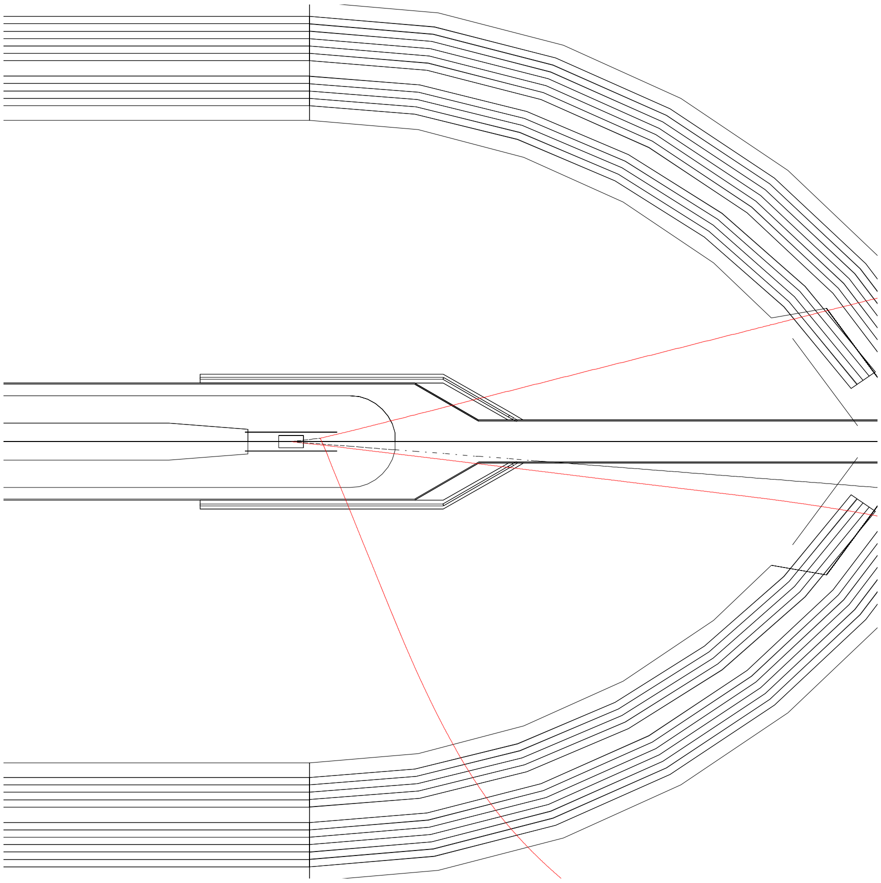

Figure 16: GEANT simulation of $\gamma p \rightarrow K^0\Sigma^+$ showing the inner part of the CLAS detector (Start Counter array and Region 1 drift chambers) and the proposed frozen spin target cryostat, coils, and cell.

In the first study we investigated the optimal field setting of the CLAS torus magnet by generating events at 4 positive and 4 negative field settings. For six photon energies 20000 $K^+\Lambda$ events were thrown, the decay mode of Λ was set to $\Lambda \rightarrow p\pi^-$. These events were mixed with 20000 events of the reaction $\gamma p \rightarrow K^+\Sigma^0$ with Σ^0 decaying into $\Lambda\gamma \rightarrow p\pi^-\gamma$. As background processes the same amount of $K^+\Lambda$ and $K^+\Sigma^0$ events as well as 50000 events of the reaction $\gamma p \rightarrow p\pi^+\pi^-\pi^0$ (phase space distribution) were generated allowing for Fermi motion of nucleons in butanol. Please note that the amounts of simulated events do not reflect the relative cross sections for these reactions.

The positively charged final state particles, K^+ and proton, were identified via time-of-flight and fully reconstructed tracks in the CLAS drift chamber system. The cut on the reconstructed mass for proton was set to $0.83 < m_p < 1.04$ GeV and for kaon was set to $0.38 < m_K < 0.65$ GeV. The hyperon was identified in the missing mass distribution $MM(\gamma p \to K^+X)$. In order to reduce the background from misidentified particles and from reactions on bound nucleons we cut on the missing mass distributions for Λ ($1.10 < MM(\gamma p \to K^+X) < 1.133$ GeV) and for Σ^0 ($1.176 < MM(\gamma p \to K^+X) < 1.208$ GeV). Figure 17 shows the mass spectrum of reconstructed charged particles and the missing mass distribution $MM(\gamma p \to K^+X)$ for generated events at $E_\gamma = 1.45$ GeV and $B = 0.4 \times B_0$. Due to the applied mass cuts the contamination of the 3π background is small. For real data we expect a larger contamination from misidentified pions due to the $40\times$ higher cross section for multi-pion reactions which is not reflected in our simulation; nevertheless, since the distribution of this background under the Λ and Σ^0 signals is smooth, this kind of background from multi-pion productions can easily be separated. A more severe contamination is caused by strangeness reactions produced on bound nucleons which dominates the background distribution (*dotted curve*) in Fig. 17.

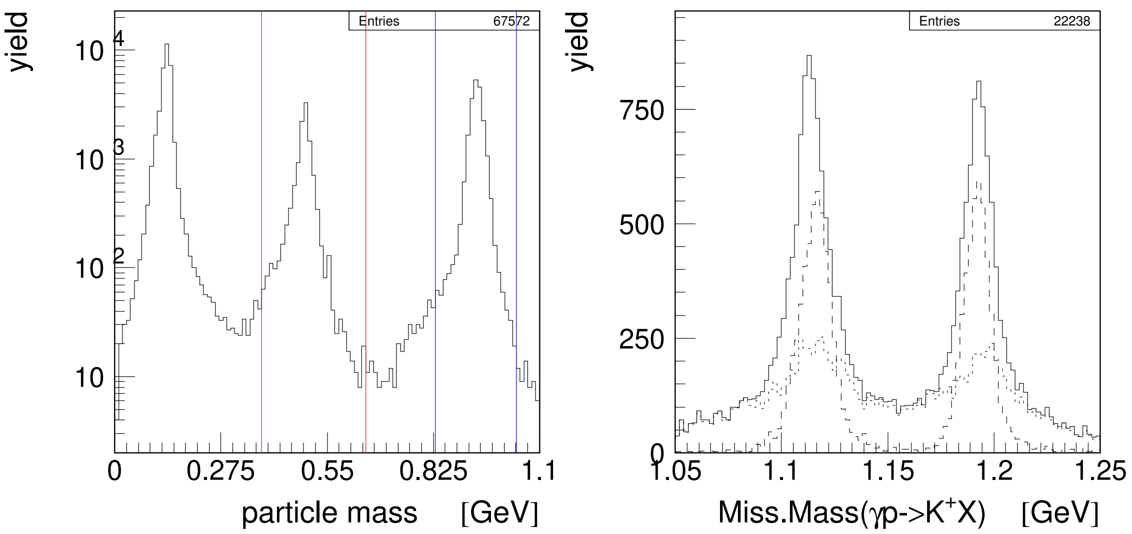

Figure 17: Reconstructed particle masses for simulated data at $E_\gamma = 1.45$ GeV and $B = 0.4 \times B_0$ on the *left* and missing mass MM($\gamma p \to K^+X$) for the same data set on the *right*. The contributions from $K^+\Lambda$ and $K^+\Sigma^0$ produced on free nucleons is indicated as *dashed* distribution, the contributions from kaon production on bound nucleons and misidentified pions as *dotted* line.

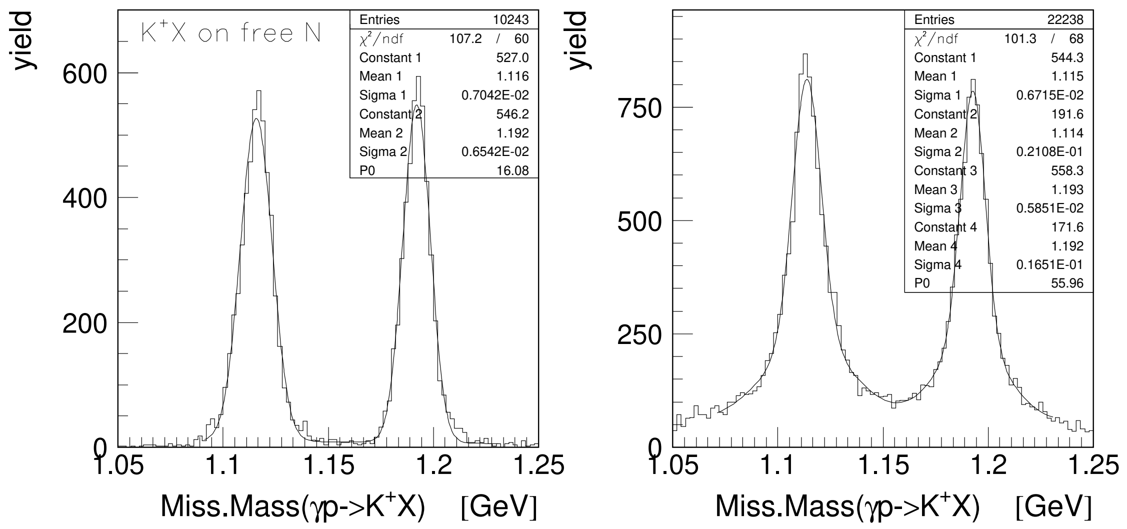

Figure 18: Convoluted fit of missing mass MM($\gamma p \rightarrow K^+X$) for the same data set as in Fig. 17. The distribution on the *left* shows the missing mass for kaons produced on free nucleons with Gaussian fits on the Λ and Σ^0 signals, on the *right* the corresponding distribution with background.

The distributions are broader than those of corresponding reactions on free nucleons and can be estimated via a convoluted fit assuming a Gaussian distribution for the reaction on free nucleons and a second broader Gaussian distribution for the production on bound nucleons as shown in Fig. 18. Nevertheless, for real data taking it will be necessary to take a sufficient amount of data on a carbon target; see Sec. 4.1 for details.

The resolution for the Λ and Σ^0 peak depends on the strength of the magnetic field as well as the average momentum of the K^+. The missing mass resolution for both hyperon states is considerably worse for the low field setting ($B/B_0 = 0.25$). The resolution remains almost constant for the high field; on the other hand, we found a slightly lower acceptance for K^+ and K^+p in this case. Furthermore, the acceptance for detecting the decay pions from $\mathrm{K}^0 \rightarrow \pi^+\pi^-$ in the reaction $\gamma p \rightarrow \mathrm{K}^0\Sigma^+$ is considerably reduced.

Figure 19 shows the overall acceptance for proton, K^+, and K^+p in the mass range of Λ as functions of the torus field setting. The CLAS acceptance for K^+ and proton is almost constant for all positive torus field settings (positively charged particles bent outwards). At high field ($B = 0.9 \times B_0$) the acceptance for K^+p is slightly reduced, especially for the lower energies. For negative torus field settings the overall acceptance is very low for photon energies below $E_\gamma \simeq 1.8$ GeV. Moreover, the angular range of the acceptance is considerably reduced to $\approx$ 60–130°. As result of our study, we propose to perform the experiment at a torus field between 0.4 and $0.6\times B_0$.

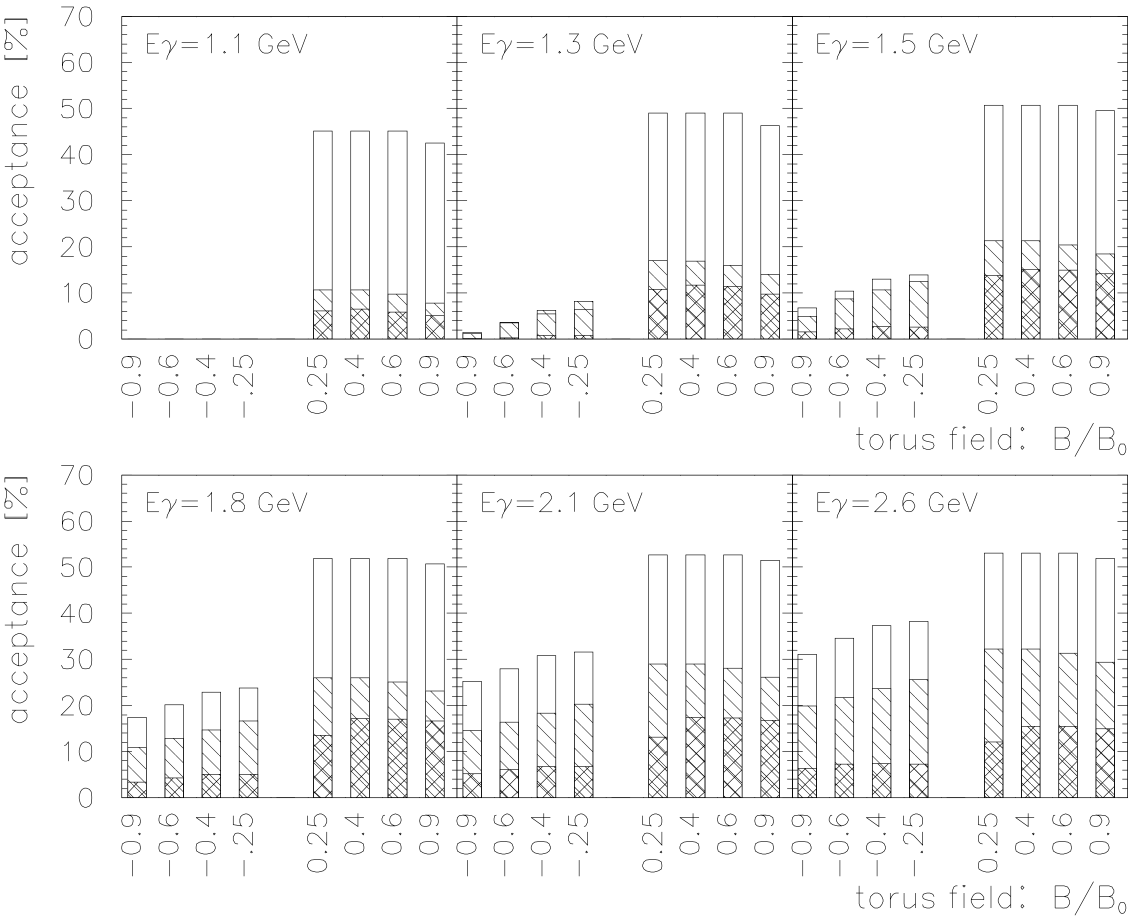

Figure 19: CLAS torus field dependence of the acceptance of K^+, p, and K^+p from the reaction $\gamma p \rightarrow \mathrm{K}^+\Lambda$. The *white* bars represent the overall CLAS acceptance for protons, the *hatched* bars for K^+, and the *dense hatched* bars for K^+p.

In a second study we repeated the simulation of $\gamma p \rightarrow \mathrm{K}^+\Lambda$ for the torus field setting $B = 0.5 \times B_0$. For fixed photon energies we determined the acceptance of K^+, proton, and combined K^+p as function of the kaon production angle $\theta_{cm}(K^+)$. The results shown in Figure 20 are based on 200,000 generated events of the reaction $\gamma p \rightarrow \mathrm{K}^+\Lambda$ per energy setting.

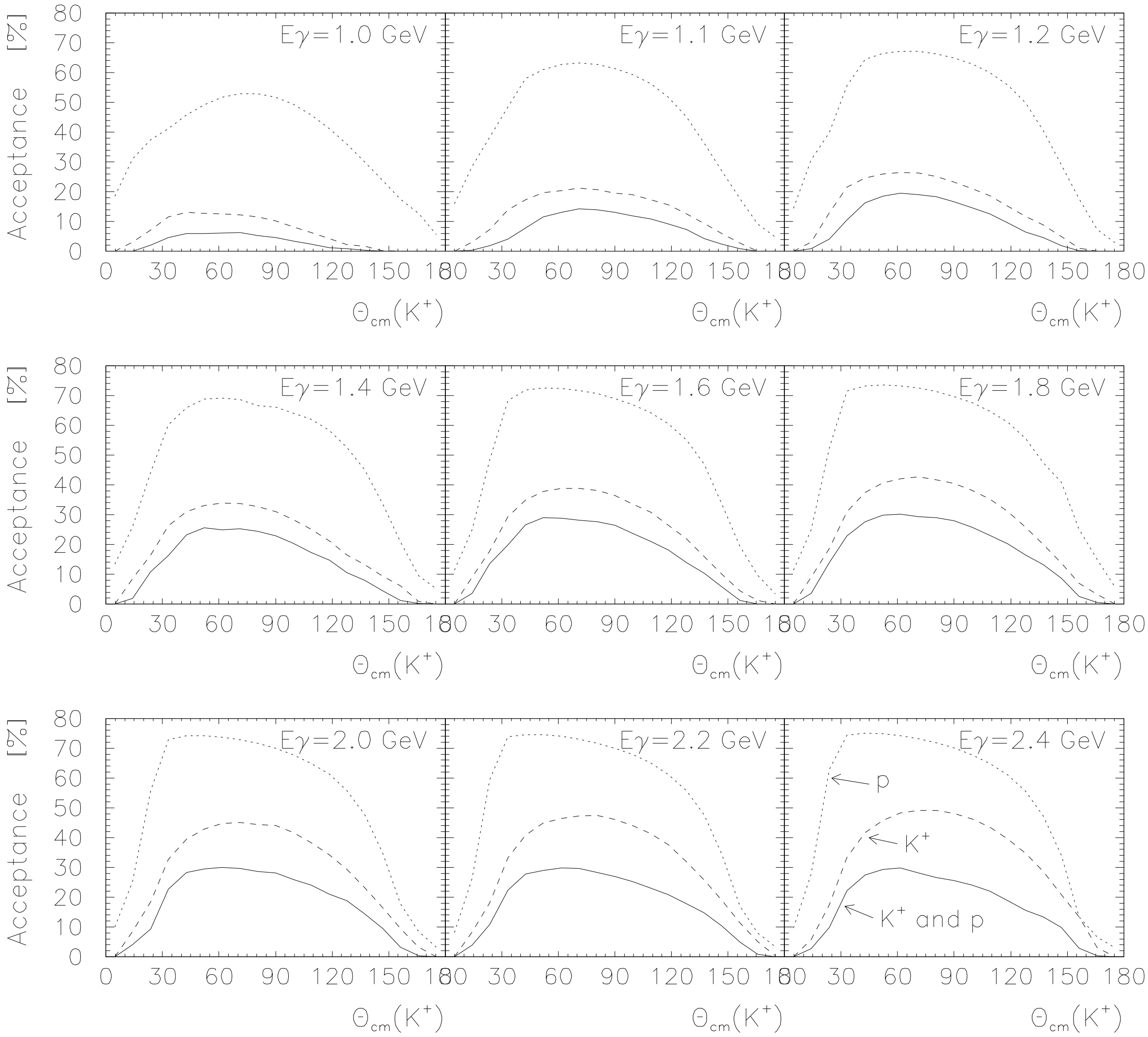

Figure 20: CLAS acceptance of K^+, p, and K^+p for the reaction $\gamma p \rightarrow \mathrm{K}^+\Lambda$ at a torus field of $0.5 \times B_0$. *Dotted line:* acceptance of p, *dashed line:* acceptance of K^+, *solid line:* acceptance of K^+p in the mass range of Λ.

A third study was carried out to test for one energy bin how well the signal can be extracted and polarization observables can be reproduced given a generated event distribution according to

$$\frac{d\sigma}{d\Omega} = \frac{d\sigma_0}{d\Omega}(1 + P_y T) \ , \tag{5}$$

where $d\sigma_0/d\Omega$ is the unpolarized cross section, P_y the degree of transverse polarization of the target proton (perpendicular to the scattering plane), and T the target asymmetry. We assumed the frozen spin target to be polarized by 90%. The input data followed the cross section and target asymmetry parametrization of the Mart-Bennhold model – with $D_{13}(1960)$ included – at a photon energy of 1.45 GeV ($W = 1.9$ GeV). 30,000 $K\Lambda$ events on free protons were generated, 1/3 with the target polarization along the normal to the scattering plane, 2/3 opposite to the scattering plane, as shown in the cross section decomposition on the upper plots in Fig. 23. Additionally, 200,000 $K\Lambda$ events were generated allowing for Fermi motion.

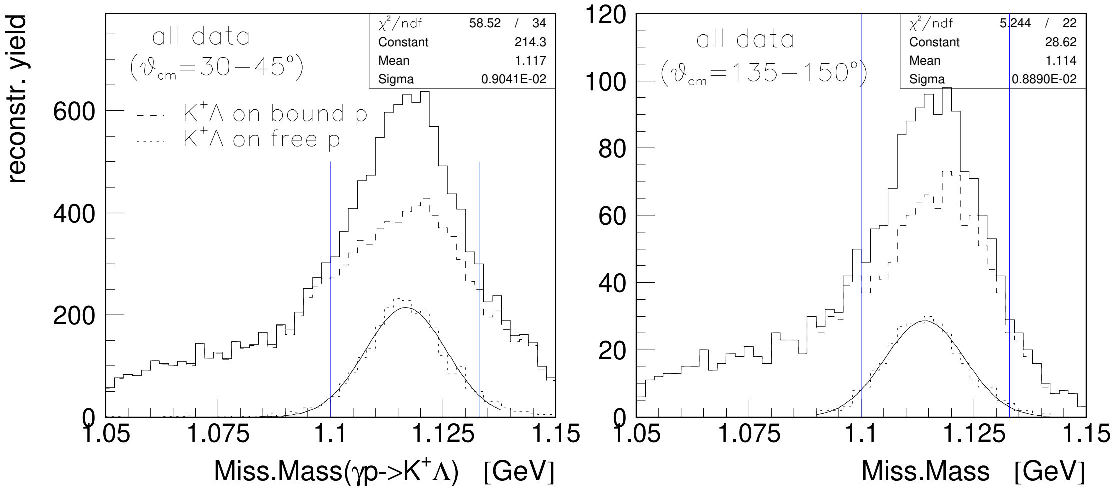

Figure 21: Missing mass spectra for simulated data showing the extraction of the effective dilution factor via subtraction of the $K\Lambda$ background produced on bound nucleons (*dashed curve*). The resulting $K\Lambda$ yield on free protons is shown as *dotted* curve. Left-hand side: for a more forward angular bin (30–45^o); right-hand side: for a backward bin (135–150^o).

Figure 21 shows the reconstructed yields in two angular bins, one in more forward direction ($30^o < \theta_{cm}(K^+) < 45^o$) with high statistics, the other in backward direction ($135^o < \theta_{cm}(K^+) < 150^o$) where the data extraction suffers from low statistics. In the mass range of Λ, indicated by vertical bars, the ratio of background to signal is $r_b \approx 2.4$ for the forward bin and $r_b \approx 2.5$ for the backward bin. The effective dilution factor amounts to $D_{eff} = 1 + r_b \approx 3.4 - 3.5$. Here, we assume

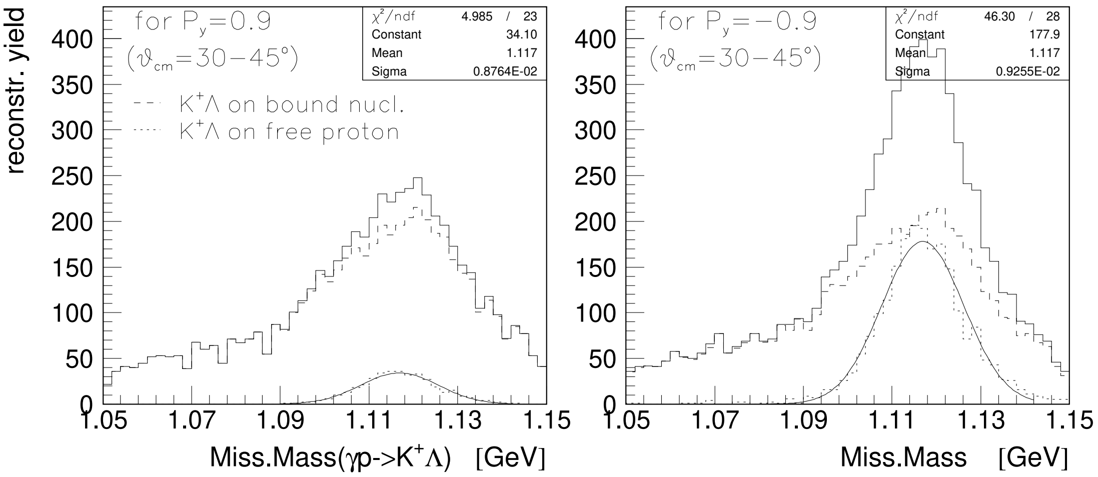

Figure 22: Missing mass spectra for one angular bin ($30^o < \theta_{cm}(K^+) < 45^o$) for both target polarization states ($P_y = \pm 0.9$). The $K\Lambda$ background produced on bound nucleons is shown as *dashed curve*, the $K\Lambda$ yield on free protons as *dotted* curve.

that the (*dashed*) distribution for events from bound nucleons is known from $K\Lambda$ production on a carbon target. Figure 22 shows the corresponding spectra for both polarization states. Due to the lower statistics, the separation would be more uncertain; therefore we take the reconstructed yields for both polarization states (N^+ and N^-) and correct them for the effective dilution factor (and the target polarization):

$$T = \frac{D_{eff}}{P_y}\frac{N^+ - N^-}{N^+ + N^-} \ , \tag{6}$$

to yield to the target asymmetry which is compared to the input data on the bottom right plot in Fig. 23.

Similar simulations were performed for the cross section decomposition according to the following equations which mark the dependence of the measured cross section on the double polarization observables E and H. This data was used to estimate the projected statisical errors in Table 2 and Fig. 11.

$$\frac{d\sigma}{d\Omega} = \frac{d\sigma_0}{d\Omega}(1 - P_\lambda P_z E) \ , \tag{7}$$

$$\frac{d\sigma}{d\Omega} = \frac{d\sigma_0}{d\Omega}(1 - P_{lin} P_x H \sin 2\varphi) \ , \tag{8}$$

where P_z is the degree of longitudinal polarization of the target protons, P_x the transverse in-plane polarization of the target, P_λ the degree of circular polarization of the beam photons, and P_{lin} its linear polarization; φ is the angle between the photon polarization vector $\vec{\epsilon}$ and the reaction plane.

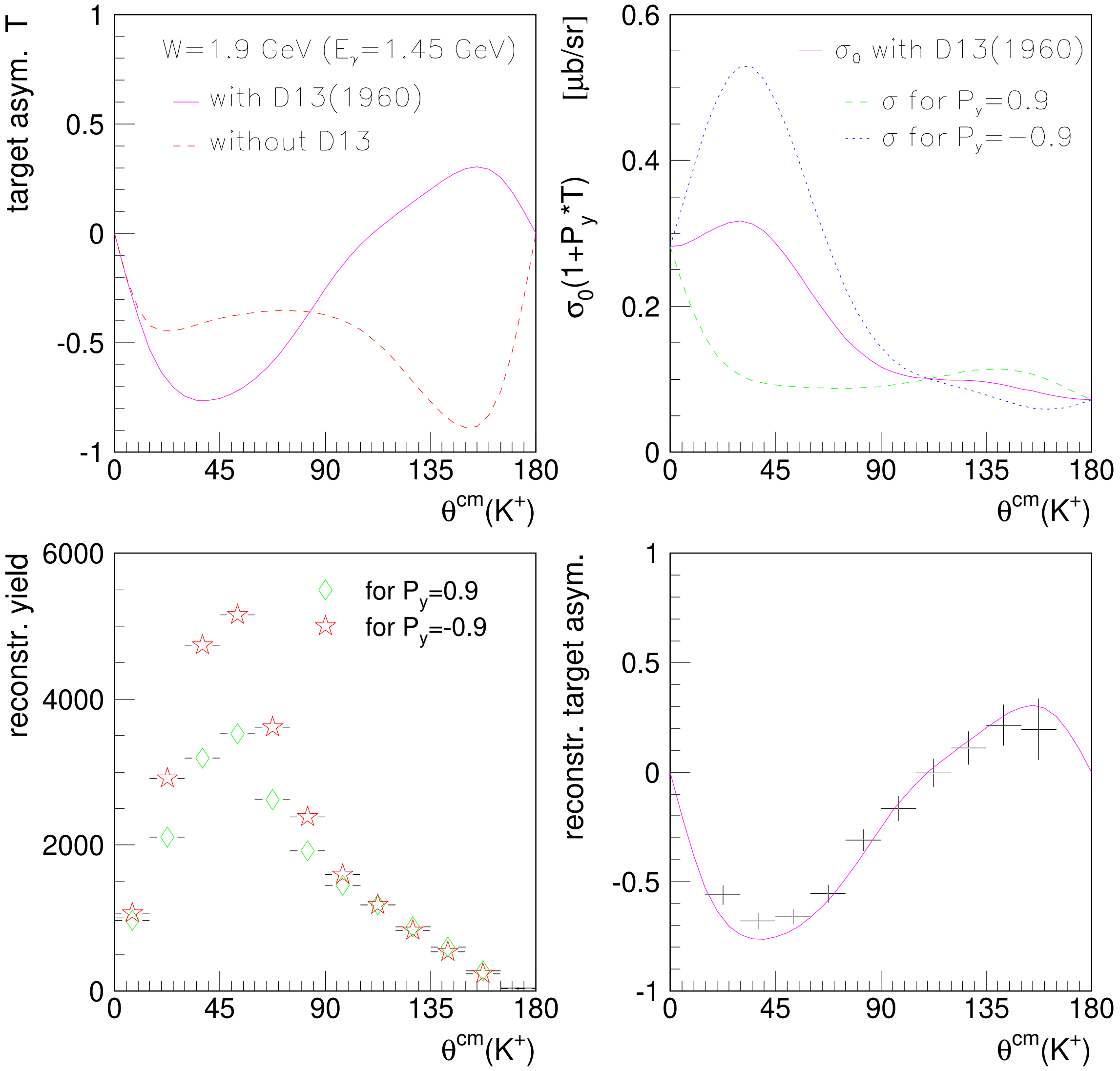

Figure 23: Study to reconstruct the target asymmetry T: predicted value of T according to the Mart-Bennhold model (*top left*); modulation of differential cross section with T (*top right*); reconstructed yield for both polarization states (*bottom left*); the reconstructed target asymmetry (*bottom right*) using an effective dilution factor of $D_{eff} = 3.5$ as determined from Fig. 21.

3.2 Process identification in CLAS-g1 data

Data for the reaction $\gamma p \to K^+\Lambda$, $\gamma p \to K^+\Sigma^0$, and $\gamma p \to K^0\Sigma^+$ were taken at Jlab with CLAS in 1998 and 1999 as part of the g1 running period. During the first run in 1998 the photon beam was unpolarized, during the other run periods the beam was circularly polarized. The analysis of these reactions is underway. As a preliminary result the total cross section was shown in Figure 1.

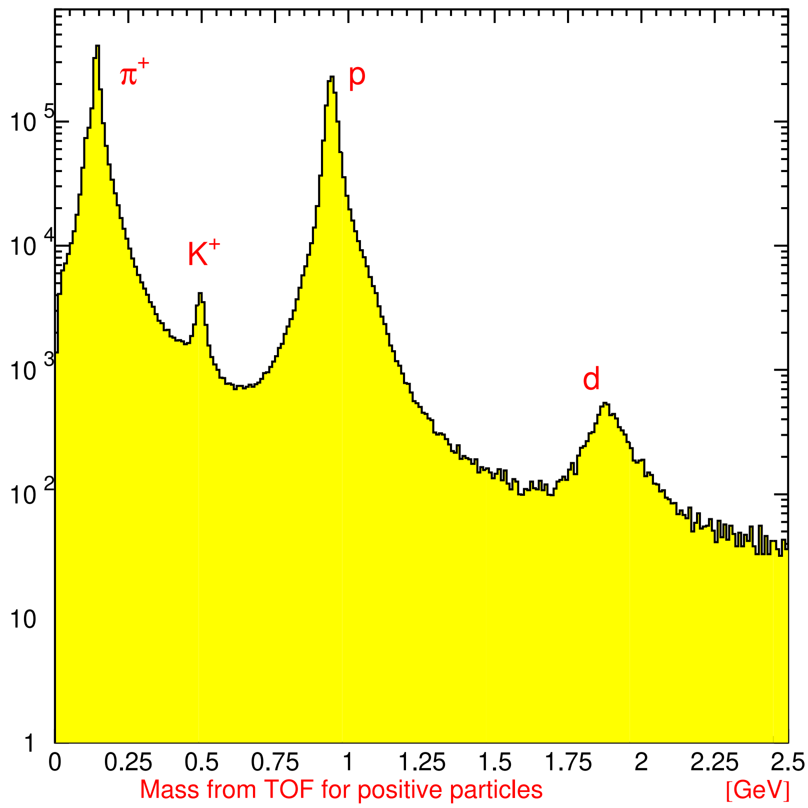

Figure 24: CLAS g1c data: Reconstructed masses of positively charged particles.

By means of our analysis routines developed for the acceptance studies we analyzed a small fraction (ca. 5%) of the g1c data set. The K^+ was identified via cuts in the reconstructed mass spectrum shown in Fig. 24. The kaon (m_K = 0.495 GeV) is clearly visible in the distribution despite of the π^+ background. Figure 25 shows the resulting missing mass distribution in the mass range below 1.25 GeV. The signals of Λ and Σ^0 appear at $MM(\gamma p \to K^+X) \approx 1.117$ GeV and 1.192 GeV, respectively. The two states are well separated although some contamination from the (mostly flat) background is expected.

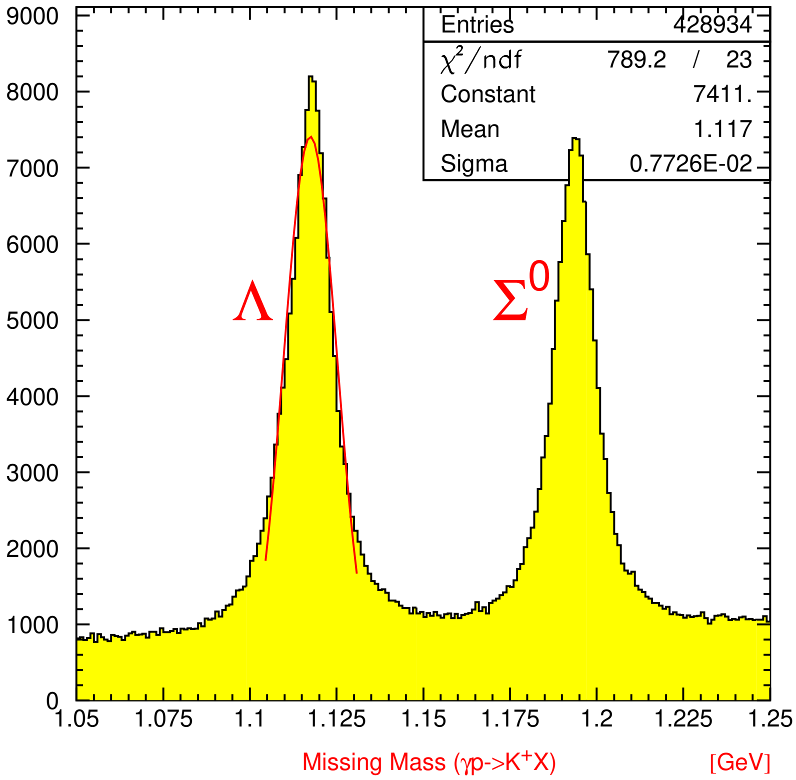

Figure 25: CLAS g1c data: Missing mass distribution for $\gamma p \to K^+X$. The Λ and Σ^0 peaks at ≈ 1.117 GeV and 1.192 GeV, respectively, are well separated.

For events where a coincident proton was reconstructed, the missing mass of the K^+p system is plotted in Figure 26. A loose cut on the dominating π^- signal ($0.11 <$MM$(\gamma p \to K^+X) < 0.17$ GeV) results in a missing mass distribution of $\gamma p \to K^+X$ showing a Λ signal without major background.

The extraction of the hyperon signals from missing mass distributions is obviously feasable with data from photoproduction experiments at CLAS. The background from misidentified particles appears as mostly smooth distribution which easily can be separated via further cuts.

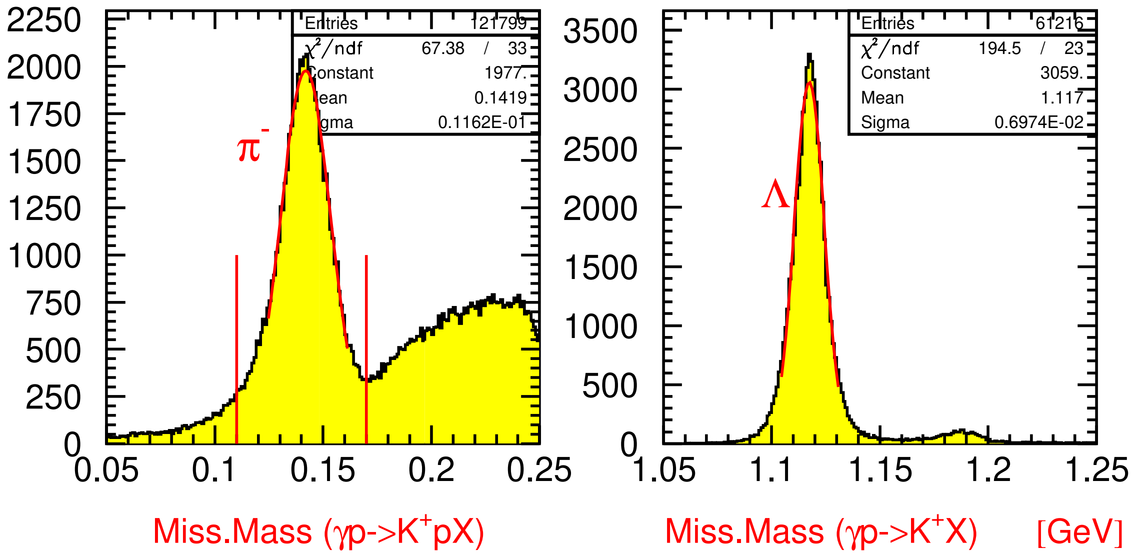

Figure 26: CLAS g1c data: Missing mass distribution for $\gamma p \to K^+ pX$ (*left*) and missing mass distribution for $\gamma p \to K^+ X$ for events with detected K^+ and p (*right*).

4 Experimental Parameters

4.1 Target Parameters

We propose to construct a frozen spin target for use in photon-induced experiments with CLAS. The dynamically polarized target used for electron-beam experiments at CLAS has the disadvantage that it requires the target to be located inside a strong (B$\approx$ 5 T) and very uniform (ΔB/B$\approx 10^{-4}$) magnetic field. The magnet needed to produce this field occupies a major fraction of the space around the target sample, leaving only a relatively small acceptance for outgoing particles, and the useful acceptance for low-momentum charged particles is further reduced by large deflections in the strong magnetic field. For experiments using a large-aperture spectrometer like CLAS in conjunction with a tagged photon beam, which deposits negligible energy in the target, a more attractive option is to use a frozen spin polarized target.

In a frozen spin target, the material is polarized in the standard way with microwave irradiation in a high magnetic field. Then, with the microwave off, the temperature of the material is lowered as much as possible, so that the relaxation time of the polarization becomes very long, hence the term "frozen spin". The value of the relaxation time is a strong function of the ratio B/T where B is the value of the magnetic holding field and T the material temperature. By operating at a sufficiently low temperature, it is possible to reduce the holding field to less than 0.5 T and modest uniformity, while still preserving a high polarization for times acceptable for running the experiment.

The low holding field can be supplied either by the fringe field of the polarizing magnet or by another magnet, the geometry of which can be tailored to the particular experiment to provide a much larger acceptance than obtainable with a high-field magnet. For example, the polarized target for the Bonn–Mainz GDH experiments [47] uses a longitudinal holding field produced by a very thin (500μm) superconducting solenoid located within the target cryostat which offers virtually no obstruction to the outgoing particles. Another arrangement may be solenoids in a certain distance from the target along the beam axis which do not obstruct the geometrical acceptance of the spectrometer. For transverse polarization, a suitable holding field could be produced by a pair of superconducting Helmholtz coils parallel to the beam axis, also contained within the target cryostat. Figure 27 shows a rough sketch of the holding magnets envisioned for CLAS. The coils could be positioned as much as possible within the shadows of the CLAS torus, to minimize the loss of acceptance.

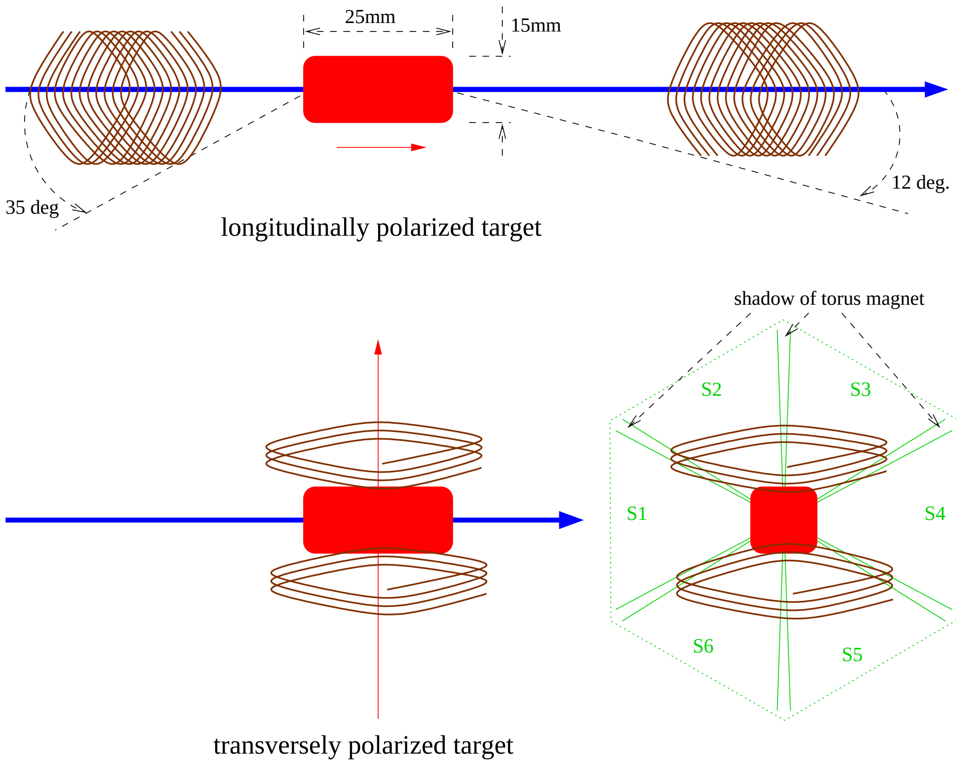

Figure 27: Sketch of the frozen spin target for CLAS.

A "standard" frozen spin target such as the Bonn target uses butanol as target material. Doped polyethylene as another possible target material is under study at Nagoya University [48]. Considering the achievements so far, we propose to use butanol (C_4H_9OH) which has a density of 1.5 g/cm^3 and a dilution factor of $D = 7.4$.

A dilution refrigerator is used to provide the lowest temperatures and reasonable cooling power when polarizing. Typical values [49] would be 50 mK for frozen spin operation and 200–400 mK with $\approx$ 50 mW cooling power when polarizing. The University of Virginia (UVa) has the capability of providing such a refrigerator which can be assembled from major components currently in its laboratory. This dilution refrigerator was fabricated at CERN but never assembled; however, three others of the same design have been used very successfully in other experiments at the CERN PS and LEAR.

Other typical parameters for the system are [50]: a 2.5 T polarizing magnet, microwave frequency of 70 GHz to polarize, and a standard Liverpool Q-meter to measure the polarization to a accuracy of about 3%. For a butanol target, proton polarizations of about 90% with hold times of around 200 hours are achievable, while deuteron polarizations for deuterated butanol could reach

50% with long hold times.

We propose to construct a cylindrical butanol target of 25 mm length and 12–15 mm diameter. The proposed target size reflects a consideration to reduce energy loss and multiple scattering while ensuring the beam size being smaller than the target. In order to determine the effective dilution factor D_{eff}, we propose to collect data simultaneously at 50% event rate on unpolarized material by placing a carbon target ($\rho = 2.26$ g/cm^3) of 8.3mm length at a slightly downstream position. Addtionally, we propose to take data on an unpolarized sample during the times needed to re-polarize the target.

This target system could efficiently be produced by a collaboration between the Jefferson Lab target group, University of Virginia, and University of South Carolina.[8] Such a target system – especially if transverse polarizations are accommodated – would be a flexible facility for a wide range of polarization experiments with CLAS.

4.2 Photon Beam Parameters

In order to extract double polarization observables involving polarized target and polarized beam, we propose to perform the experiment in **two separate sections**:

- During one run period we will employ circularly polarized photons produced by bremsstrahlung off longitudinally polarized electrons on an amorphous radiator. The polarization is approximately [9] given by

  $$P_{circ} = P_{el}(4x - x^2)/(4 - 4x + 3x^2)$$

  where $x(= k/E_0)$ is the ratio of photon energy (k) and electron energy (E_0), and P_{el} is the degree of longitudinal polarization of the incident electrons. The degree of polarization rises with x to $0.996 \times P_{el}$ at $x = 0.95$. Since $P_{circ}/P_{el} < 60\%$ for $x < 0.5$, it is desirable to trigger only on the high energy photons, i.e. the upper part of the tagging hodoscope.

  Since the angular spread of incoherent bremsstrahlung results in a beam that is larger than the target, the photon beam aperture has to be reduced. We will use the existing instrumented collimator ($r = 1$ mm) – positioned 16 m from the target – which, additionally, allows the photon beam position to be monitored. The collimation diminishes the photon flux on the target significantly: for $E_0 = 1.6$ GeV to 32% and for $E_0 = 2.6$ GeV to 47% of the

[8] The nuclear physics group at SC recently hired a cryotarget expert as Postdoc to be assigned to this project.

[9] A more precise calculation requires angular integration over the collimation aperture.

uncollimated flux.[10] We estimated the photon flux assuming a 15 nsec time window for the coincidence between tagger hodoscope and CLAS start counters.[11] For $E_0 = 1.6$ GeV and photons tagged between 1.10 GeV and 1.52 GeV (upper 35% of the Hall-B tagging hodoscope) the calculated collimated photon flux is 5.6 MHz for 17.5 MHz tagging rate in this tagging range, corresponding to 50 MHz on the whole tagger, with an accidental rate of ca. 80%. For $E_0 = 2.6$ GeV and $1.50 < E_\gamma < 2.47$ GeV (upper 49% of the tagger) the collimated photon flux amounts to 11.5 MHz for 24.5 MHz tagging rate with an accidental rate of ca. 65%.

- During another run period we will use linearly polarized photons produced by coherent bremsstrahlung on a thin diamond. Coherent bremsstrahlung has been successfully employed at Jefferson Lab during the first part of the CLAS-g8 run period. The degree of linear polarization for a small photon energy range at the coherent edge depends heavily on the collimation aperture and on the fractional photon energy $x = k/E_0$. Production on a diamond with a thickness of 20μm yields 70% at $x = 0.5$ and a collimation of one characteristic angle ($\theta_{char} = m_e c^2/E_0$). The degree of polarization increases with lower fractional energy, e.g. to 92% at $x = 0.3$ and the same collimation. The polarization of the collimated beam is fairly constant over a 200 MeV energy range near the coherent edge.[12]

4.3 Trigger

The trigger for this experiment requires the detection of at least one charged particle in the CLAS detector. For the reaction channels $\mathrm{K}^+\Lambda$ and $\mathrm{K}^+\Sigma^0$ this particle must be the K^+. For the reaction $\gamma p \rightarrow \mathrm{K}^0\Sigma^+$ both charged pions from the decay $\mathrm{K}^0 \rightarrow \pi^+\pi^-$ have to be detected in CLAS.
In order to measure polarization observables which involve the polarization state of the recoiling hyperon, one has to detect additionally one of the decay particles: preferably the positively charged particle from the decays $\Lambda \rightarrow \mathrm{p}\pi^-$, $\Sigma^+ \rightarrow \mathrm{p}\pi^0$, $\Sigma^+ \rightarrow \mathrm{n}\pi^+$.

The trigger condition is consistent with the required trigger setting in the GDH experiment E01-104 [52]. This allows for sharing beam time with circularly polarized beam on longitudinally polarized target. Additionally, the open trigger allows for simultaneous measurement of polarization observables in $\gamma p \rightarrow \eta p$, $\gamma p \rightarrow \eta' p$, $\gamma p \rightarrow \pi N$, $\gamma p \rightarrow \rho^0 p$ $\gamma p \rightarrow \rho^+ n$, $\gamma p \rightarrow \omega p$, and other channels.

[10] The corresponding collimation is $0.78\times\theta_{char}$ and $1.27\times\theta_{char}$, respectively. The fraction of photons after collimation varies slightly with photon energy by ca. $\pm1.5\%$ for $x \simeq 0.5$ to $x \simeq 0.95$.

[11] Currently, the coincidence window is 20 nsec when the whole tagging hodoscope is used.

[12] The degree of polarization diminishes by less than 5% at 200 MeV below the coherent edge energy.

4.4 Count Rate Estimate

We will have to perform the hyperon analysis over a large photon energy range in order to determine the energy dependent strengths of various partial waves. In order to allow for discrimination between various solutions of partial wave and pole fits it is required to measure single and double polarization observables to a high accuracy (± 0.05) in the energy range around the resonant structures. On the other hand, the whole energy range has to be explored for possible resonant structures. Since one of the photon beam settings described in Sec. 4.2 covers naturally a large energy range, whereas the other focuses on small ranges which are solely determined by the orientation of the diamond radiator, it is convenient to employ a beam of circularly polarized photons to measure polarization observables with high precision within a coarse segmentation in $\theta_{cm}(K)$ (9 bins of 15^o) and center-of-mass energies W between 1.71 GeV and 2.36 GeV (26 bins of 25 MeV). In the second run period – using coherent bremsstrahlung photons – small energy ranges will be studied allowing a fine segmentation in W and higher precision of the corresponding polarization observables. Within each energy bin the observables will be extracted as functions of the kaon production angle $\theta_{cm}(K^+)$ (resp. $\theta_{cm}(K^0)$ for $K^0\Sigma^+$ production) in the range of 15–165° (i.e. -0.966$< \cos\theta_{cm}(K) < 0.966$),[13] for energies below $E_\gamma = 1.4$ GeV in the range of 15–150°.

Figure 1 shows that the total cross section for $\gamma p \to K^+\Lambda$ at center-of-mass energies between 1.7 GeV and 1.9 GeV is almost flat at $\sigma \simeq 1.8\mu$b, and decreases to $\sigma \simeq 0.5\mu$b at $W = 2.3$ GeV. For a photon rate Φ at the target of 5.6 MHz within a tagged energy range of 1.1 GeV to 1.52 GeV and a 2.5 cm long butanol target (ρ_{tg}=1.5 g/cm^3, dilution factor $D = 7.4$) we expect

$$N_{evts} = \sigma\Phi\rho_{tg}l_{tg}N_A/D \quad \approx 3.1 \text{ events/sec}$$

produced on free target protons for $W < 1.9$ GeV. The rate is expected to decrease to ≈ 1 event/sec at $W \simeq 2.3$ GeV.[14] We expect a similar rate for $K^0\Sigma^+$ production and half of the rate for $\gamma p \to K^0\Sigma^+$.

In order to optimize the acceptance and resolution for positively charged particles, we propose to set the magnetic field of the CLAS torus to half of its maximum value. The measurements of target asymmetry and beam–target polarization observables require the detection of a single K^+ whereas the detection of both positively charged particles, K^+ and p, is required for measuring the double polarization observables T_x, T_z, L_x, and L_z which involve the Λ recoil polarization.

[13] The very forward and backward directions cannot be measured with CLAS.

[14] Since the collimated photon flux for $E_0 = 2.6$ GeV is significantly higher, the integrated event rate for $1.9 < W < 2.35$ GeV is expected to be ≈ 4.1 events/sec, despite of the lower cross section.

During the first run period, using circularly polarized beam and longitudinally polarized target, we will run at two different electron energies, $E_0 = 1.6$ GeV and $E_0 = 2.6$ GeV, in agreement with E01-104. Taking into account the decrease of photon polarization with lower photon energy, we want to extract the polarization observables in the following energy ranges:

- During the 1.6 GeV run we want to measure at center-of-mass energies between 1.705 GeV and 1.930 GeV which corresponds to the photon energy range $1.08 < E_\gamma < 1.52$ GeV (covering the upper 38% of the Hall-B tagger). Taking into account the acceptance of CLAS for K^+ and proton (cf. Fig. 20), we expect the following yields per W-bin for 24 hours of beam time: $\approx$ 3800–7100 events with K^+ candidates and $\approx$ 2000–5400 events with coinciding K^+ and p.

- During the 2.6 GeV run we want to measure in the energy range $1.92 < W < 2.34$ GeV which corresponds to $1.5 < E_\gamma < 2.47$ GeV (covering the upper 50 % of the Hall-B tagger). For this energy range the projected yields per W-bin for 24 hours of beam time vary significantly due to the variation of the cross section: $\approx$ 1700–7400 events with K^+ candidates and $\approx$ 1500–5500 events with coinciding K^+ and p.

In order to perform measurements in more than one combination of target and beam polarization, we propose to use a linearly polarized beam and a transversely polarized target during the second run period. Together with the beam-target asymmetry H we will extract T_x and T_z by analyzing the angular distribution of the proton from Λ decay. The target asymmetry T is measured simultaneously by summing over the beam polarization states.[15] We propose to vary the position of the coherent edge in steps of 170 MeV photon energy which requires 8 settings to cover the photon energy range between 1.15 GeV to 2.5 GeV (i.e. $1.73 < W < 2.36$ GeV). In the case of coherent bremsstrahlung the collimated photon beam will will yield a photon flux on target of $\approx 6 \times 10^6$ Hz for 30 MHz tagging rate, over 80 % of the photons on target having an energy within the 200 MeV photon energy interval of high polarization. We expect an energy dependent count rate of ca. 0.3–1.6 events/sec for $K\Lambda$ candidates produced on free protons within the 200 MeV energy interval below the coherent edge. Taking into account the detector acceptance, yields of $\approx$ 1900–6600 events with K^+ candidates and $\approx$ 1200–5000 events with coincident K^+ and p per W-bin, are expected for 24 hours of beam time.

For an evaluation of the statistical error we take into consideration that the yield of events produced on a free target proton is only a fraction of the total yield which depends on the degree

[15] T can be measured with unpolarized beam as well, but this would require additional beam time.

of polarization of beam and target and the effective dilution factor which is given by the fraction of all events after kinematic cuts – including those from bound nucleons – and of all events from free protons. Additionally, the above mentioned yield has to be divided into two parts (N^+, N^-); this is obvious for single polarization observables, but double polarization observables (A^{ik}) are defined in a similar way: (a) the yield for parallel settings where the projections of the polarization vectors onto the corresponding axes are both positive or both negative ($N_{\|} = N^{++} + N^{--}$), and (b) the yield for opposite settings where projection of one polarization vector is in positive directions, the projection of the other one in the corresponding negative direction ($N_{\perp} = N^{+-} + N^{-+}$):

$$A^{ik} = \frac{D_{eff}}{P_b P_{tg}} \frac{N_{\|} - N_{\perp}}{N_{\|} + N_{\perp}} \ , \quad \delta_{stat} A^{ik} \simeq \frac{D_{eff}}{P_b P_{tg}} \frac{1}{\sqrt{N_{\|} + N_{\perp}}} \quad . \tag{9}$$

The statistical error is dominated by the uncertainty on subtracting the total yields (numerator); in comparison, the effective dilution factor (D_{eff}) which is extracted from missing mass spectra for carbon data, i.e. proportional to $N_{total} \simeq N_{\|} + N_{\perp}$, contributes only to ca. 1–2%.[16] Table 2 shows the estimated statistical uncertainties on E and H for 3 energy bins. For E – to be measured during the first run period with circularly polarized beam and longitudinally polarized target – we assume 25 days of beam time for $W \simeq 1.74$ GeV and $W \simeq 1.92$ GeV and 27 days of beam time for $W \simeq 2.24$ GeV. For H – to be measured during the second run period with linearly polarized beam and transversely polarized target – we assume 5 days of data taking for each energy interval. The frozen spin target is assumed to be 90% polarized during both run periods and the polarization of the primary electron beam during the first run period to be 75%. The underlying yields for the angular bins are based upon the Mart-Bennhold model.

The systematic error is dominated by the uncertainties of the measurements of beam and target polarization and the estimation of the effective dilution factor. We estimate the uncertainty on D_{eff} to be of the order of 3–4%. The target polarization will be determined to 3–4% using a Q-meter. For measurements with circularly polarized photons the beam polarization can be determined to better than 4% using a Møller Polarimeter to measure the polarization of the primary electron beam and the calculated helicity transfer. For experiments with linearly polarized photons we expect that the beam polarization being determined to 5–6% accuracy via an analysis of the photon spectrum and a photon polarimeter under construction for the second beam time period of CLAS-g8. Other

[16] We assume that the data on a carbon target taken simultaneously as well as during re-polarization times will yield roughly the same amount as the data taken on polarized butanol. For W and $\theta_{cm}(K^+)$ bins with less statistics we will combine neighbouring bins assuming that the distributions do not vary significantly in these energy and angular ranges.

Observable	E			H		
W (GeV)	1.730–1.755	1.905–1.930	2.230–2.255	1.730–1.755	1.905–1.930	2.230–2.255
E_γ (GeV)	1.126–1.173	1.465–1.516	2.182–2.242	1.126–1.173	1.465–1.516	2.182–2.242
P_b	0.66	0.74	0.63	0.93	0.84	0.72
$15^o < \theta_{cm} < 30^o$	±0.034	±0.033	±0.034	±0.039	±0.031	±0.031
$30^o < \theta_{cm} < 45^o$	±0.028	±0.026	±0.023	±0.034	±0.024	±0.021
$45^o < \theta_{cm} < 60^o$	±0.027	±0.025	±0.023	±0.033	±0.023	±0.022
$60^o < \theta_{cm} < 75^o$	±0.028	±0.029	±0.027	±0.033	±0.027	±0.024
$75^o < \theta_{cm} < 90^o$	±0.029	±0.035	±0.034	±0.034	±0.033	±0.031
$90^o < \theta_{cm} < 105^o$	±0.030	±0.042	±0.039	±0.035	±0.038	±0.038
$105^o < \theta_{cm} < 120^o$	±0.032	±0.047	±0.047	±0.037	±0.043	±0.043
$120^o < \theta_{cm} < 135^o$	±0.036	±0.055	±0.057	±0.044	±0.051	±0.052
$135^o < \theta_{cm} < 150^o$	±0.043	±0.067	±0.072	±0.052	±0.063	±0.064
$150^o < \theta_{cm} < 165^o$	±0.139	±0.100	±0.121	±0.157	±0.094	±0.110

Table 2: Expected statistical uncertainty on the double polarization observables E and H for 3 energy bins within the requested days of beam time.

factors of systematic errors like photon flux on the target ($\approx$ 5–6%), target thickness ($\approx$ 3–5%), and azimuthal acceptance of CLAS ($\approx$ 1–2%) largely cancel out in asymmetry measurements.

The resulting systematic error for double polarization observables is estimated at 5–7% when circularly polarized photon beam is involved and at 6–8% for linearly polarized beam; we expect a systematic uncertainty of 5–6% on the target asymmetry T. In order to check the consistency of our data, we will make use of the algebraic relations between the measured polarization observables (cf. Sec. A.4), and we will extract beam-recoil polarization observables from the data $(\Sigma, P, O_x, O_z, C_x, C_z)$ and compare them with results from CLAS-g1 and CLAS-g8.

4.5 Beam Time Request

The approved beam time for E01-104 [52] of 5 days at 1.6 GeV electron energy and 7 days at 2.6 GeV electron energy will be shared with the experiment.[17] **For each electron energy we request additional 20 days of beam time**. Total beam time for experiments with longitudinally polarized target and circularly polarized beam of <u>25 days at $E_0 = 1.6$ GeV</u> and <u>27 days at $E_0 = 2.6$ GeV</u> will

[17]The co-spokespersons of E01-104 agree with a slight increase of the electron energy for the second run from $E_0 = 2.4$ GeV to $E_0 = 2.6$ GeV.

allow us to determine the double polarization observables E, L_x, and L_z for the reactions $\gamma p \to K^+\Lambda$ and $\gamma p \to K^+\Sigma^0$ in 26 W-bins and 9 angular bins of θ_{cm} with an accuracy of $\pm$ 0.05 except for the most forward and backward azimuthal angles.

In a second run period we will employ a linearly polarized beam and a transversely polarized target to measure the target asymmetry T and double polarization observables H, T_x, and T_z. Coherent bremsstrahlung offers a high degree of photon polarization, which enables accurate values for polarization observables involving the beam polarization within a shorter period of data taking. The beam time for individual settings of the coherent edge energy will be adjusted between 4 and 8 days to account for the decrease of photon polarization at higher E_γ and for variations in the count rate due to cross section and CLAS acceptance. In order to cover the coherent energy settings between 1.15 GeV and 2.5 GeV with the Hall-B tagger, the electron energy has to be $E_0 \simeq 4.5$ GeV. **We request 38 days of beam time with transversely polarized target and linearly polarized beam at $\mathbf{E_0 = 4.5}$ GeV**.

Beam time request				
Observables	photon beam polarization	target polarization	E_0 (e^- polar.)	requested beam time
E, L_x, L_y $(P, C_x, C_z)^*$	circularly (P_b =63–74%)	longitudinally ($P_{tg} \simeq 90\%$)	1.6 GeV ($P_e \simeq 75\%$)	**20 days**
E, L_x, L_y $(P, C_x, C_z)^*$	circularly (P_b =55–74%)	longitudinally ($P_{tg} \simeq 90\%$)	2.6 GeV ($P_e \simeq 75\%$)	**20 days**
T, H, T_x, T_z $(\Sigma, O_x, O_z)^*$	linearly (P_b =65–93%)	transversely ($P_{tg} \simeq 90\%$)	4.5 GeV	**38 days**

* measured simultaneously for consistency checks and comparison with CLAS-g1 and CLAS-g8 results.

The proposed experiments will explore new territory in the photoproduction of strange particles in the baryon resonance region. Due to a severe lack of data, very little is known about the role of strange quarks in the decay of resonances. The CLAS detector with its large coverage of phase space and its ability to detect a wide range of particles with good resolution is ideally suited to this type of investigation. The present proposal will capitalize on these unique features and contribute new information to a fascinating topic which has yet to be explored. The requested beam time will facilitate a variety of experiments in pseudoscalar (π, η, η') and vector meson (ρ, ω, ϕ) photoproduction on polarized targets.

A Polarization observables in Kaon Photoproduction

As shown in fig. 4, the four-momenta of the incoming photon (γ), outgoing kaon (K), target proton (p), and recoiling hyperon (Y) are named p_γ, p_p, p_K, and p_Y, respectively. The variables in the center-of-mass system are written as $p_\gamma = (\nu, \vec{k})$, $p_K = (E_K, \vec{q})$, $p_p = (E_p, -\vec{k})$, and $p_Y = (E_Y, -\vec{q})$. The Mandelstam variables s, t, and u, are defined by

$$s = (p_p + p_\gamma)^2 = (p_K + p_Y)^2, \quad t = (p_\gamma - p_K)^2, \quad u = (p_p - p_K)^2 \ . \tag{10}$$

In the following definitions the differential cross section is abbreviated by

$$\sigma(B,T,R) \equiv \frac{d\sigma^{(B,T,R)}}{d\Omega}$$

where the superscripts denote:

B the polarization state of the photon <u>beam</u>: linearly $(\perp, \|, \pi/4)$ or circularly $(\lambda_\gamma = \pm 1)$;

T the polarization state of the <u>target</u> proton: spin orientation in the c.m. frame (x, y, z);

R the polarization state of the <u>recoiling</u> hyperon: spin orientation in the rest frame of the recoiling hyperon (x', y', z').

A.1 Single Polarization observables

Recoil polarization: $\mathbf{P} = \frac{\sigma(0,0,+y') - \sigma(0,0,-y')}{\sigma(0,0,+y') + \sigma(0,0,-y')}$

Beam polarization: $\mathbf{\Sigma} = \frac{\sigma(\perp,0,0) - \sigma(\|,0,0)}{\sigma(\perp,0,0) + \sigma(\|,0,0)}$

Target polarization: $\mathbf{T} = \frac{\sigma(0,+y,0) - \sigma(0,-y,0)}{\sigma(0,+y,0) + \sigma(0,-y,0)}$

A.2 Double Polarization Observables

A.2.1 Beam – Target Polarization

circ. beam – long. target polar.: $\mathbf{E} = \frac{\sigma(+1,+z,0) - \sigma(-1,+z,0)}{\sigma(+1,+z,0) + \sigma(-1,+z,0)}$

circ. beam – transv. target polar.: $\mathbf{F} = \frac{\sigma(+1,+x,0) - \sigma(-1,+x,0)}{\sigma(+1,+x,0) + \sigma(-1,+x,0)}$

lin. beam – long. target polar.: $\mathbf{G} = \frac{\sigma(\pi/4,+z,0) - \sigma(\pi/4,-z,0)}{\sigma(\pi/4,+z,0) + \sigma(\pi/4,-z,0)}$

lin. beam – transv. target polar.: $\mathbf{H} = \frac{\sigma(\pi/4,+x,0) - \sigma(\pi/4,-x,0)}{\sigma(\pi/4,+x,0) + \sigma(\pi/4,-x,0)}$

A.2.2 Beam – Recoil Polarization

circ. beam – recoil$_{\mathbf{x'}}$ polar.: $\mathbf{C_{x'}} = \frac{\sigma(+1,0,+x')-\sigma(-1,0,+x')}{\sigma(+1,0,+x')+\sigma(-1,0,+x')}$

circ. beam – recoil$_{\mathbf{z'}}$ polar.: $\mathbf{C_{z'}} = \frac{\sigma(+1,0,+z')-\sigma(-1,0,+z')}{\sigma(+1,0,+z')+\sigma(-1,0,+z')}$

lin. beam – recoil$_{\mathbf{x'}}$ polar.: $\mathbf{O_{x'}} = \frac{\sigma(\pi/4,0,+x')-\sigma(\pi/4,0,-x')}{\sigma(\pi/4,0,+x')+\sigma(\pi/4,0,-x')}$

lin. beam – recoil$_{\mathbf{z'}}$ polar.: $\mathbf{O_{z'}} = \frac{\sigma(\pi/4,0,+z')-\sigma(\pi/4,0,-z')}{\sigma(\pi/4,0,+z')+\sigma(\pi/4,0,-z')}$

A.2.3 Target – Recoil Polarization

transv. target – recoil$_{\mathbf{x'}}$ polar.: $\mathbf{T_{x'}} = \frac{\sigma(0,+x,+x')-\sigma(0,+x,-x')}{\sigma(0,+x,+x')+\sigma(0,+x,-x')}$

transv. target – recoil$_{\mathbf{z'}}$ polar.: $\mathbf{T_{z'}} = \frac{\sigma(0,+x,+z')-\sigma(0,+x,-z')}{\sigma(0,+x,+z')+\sigma(0,+x,-z')}$

long. target – recoil$_{\mathbf{x'}}$ polar.: $\mathbf{L_{x'}} = \frac{\sigma(0,+z,+x')-\sigma(0,+z,-x')}{\sigma(0,+z,+x')+\sigma(0,+z,-x')}$

long. target – recoil$_{\mathbf{z'}}$ polar.: $\mathbf{L_{z'}} = \frac{\sigma(0,+z,+z')-\sigma(0,+z,-z')}{\sigma(0,+z,+z')+\sigma(0,+z,-z')}$

A.3 Cross section and Polarization observables

Summarizing, the polarization observables in photoproduction of pseudoscalar mesons are related to photon beam, target, and recoil polarization states as shown in Table 3 (from [22]).

Photon		Target			Recoil			Target + Recoil			
	–	–	–	–	x'	y'	z'	x'	x'	z'	z'
	–	x	y	z	–	–	–	x	z	x	z
unpolarized	σ_0	0	T	0	0	P	0	$T_{x'}$	$-L_{x'}$	$T_{z'}$	$L_{z'}$
linearly polar.	$-\Sigma$	H	$(-P)$	$-G$	$O_{x'}$	$(-T)$	$O_{z'}$	$(-L_{z'})$	$(T_{z'})$	$(-L_{x'})$	$(-T_{x'})$
circularly polar.	0	F	0	$-E$	$-C_{x'}$	0	$-C_{z'}$	0	0	0	0

Table 3: Polarization observables in photoproduction of pseudoscalar mesons. The entries in brackets denote polarization observables which also appear elsewhere in the table.

There are no new polarization observables in photoproduction accessible by triple polarization experiments (beam + target + recoil polarization). In conclusion there are 16 different polarization observables for real photon experiments.

The differential cross section can be classified by 3 classes of polarization experiments:

- polarized photons and polarized target

$$\begin{aligned}\frac{d\sigma}{d\Omega} &= \sigma_0 \{1 - P_{lin}\Sigma\cos 2\varphi \\ &+P_x\left(-P_{lin}H\sin 2\varphi + P_\lambda F\right) \\ &-P_y\left(-T + P_{lin}P\cos 2\varphi\right) \\ &-P_z\left(-P_{lin}G\sin 2\varphi + P_\lambda E\right)\}\ , \end{aligned} \tag{11}$$

- polarized photons and recoil polarization

$$\begin{aligned}\frac{d\sigma}{d\Omega} &= \sigma_0 \{1 - P_{lin}\Sigma\cos 2\varphi \\ &+P_{x'}\left(-P_{lin}O_{x'}\sin 2\varphi - P_\lambda C_{x'}\right) \\ &-P_{y'}\left(-P + P_{lin}T\cos 2\varphi\right) \\ &-P_{z'}\left(P_T O_{z'}\sin 2\varphi + P_\lambda C_{z'}\right)\}\ , \end{aligned} \tag{12}$$

- polarized target and recoil polarization

$$\begin{aligned}\frac{d\sigma}{d\Omega} &= \sigma_0 \{1 + P_{y'}P + P_x\left(P_{x'}T_{x'} + P_{z'}T_{z'}\right) \\ &+P_y\left(T + P_{y'}\Sigma\right) - P_z\left(P_{x'}L_{x'} - P_{z'}L_{z'}\right)\}\ . \end{aligned} \tag{13}$$

In these equations σ_0 denotes the unpolarized differential cross section, the degree of transverse photon polarization is denoted by P_{lin}, the (right-handed) circular photon polarization by P_λ, and φ is the angle between photon polarization vector and reaction plane. The polarization states of target proton and recoiling baryon are denoted by $P_{x,y,z}$ and $R_{x',y',z'}$, respectively.

A.4 Algebraic correlations

The 16 single and double polarization observables are not independent, the redundancy is expressed in the following nonlinear relations:

$$E_z^2 + F_x^2 + G_z^2 + H_x^2 = 1 + P^2 - \Sigma^2 - T^2\ , \tag{14}$$

$$F_x G_z - E_z H_x = P - \Sigma T\ , \tag{15}$$

$$C_x^2 + C_z^2 + O_x^2 + O_z^2 = 1 + T^2 - P^2 - \Sigma^2 \tag{16}$$

$$C_z O_x - C_x O_z = T - P\Sigma\ , \tag{17}$$

$$T_x^2 + T_z^2 + L_x^2 + L_z^2 = 1 + \Sigma^2 - P^2 - T^2\ , \tag{18}$$

$$T_x L_z - T_z L_x = \Sigma - PT\ . \tag{19}$$

In order to determine the 4 complex amplitudes in eq.(2) which describe the photoproduction of pseudoscalar mesons a set of 7 measurements have to be performed.[18] These measurements have be chosen to involve single polarization observables and at least 2 groups of double polarization observables (beam–target, beam–recoil, target–recoil). The 7 independent measurements allow for determine the amplitudes up to relative phase factors [21, 54, 53]. This is a consequence of the nonlinear structure of the correlations in eq.(14), requiring at least one additional measurement to resolve the ambiguities.[19]

B Polarization observables in terms of CGLN amplitudes

The polarization observables can be written in terms of the CGLN amplitudes [23]. The differential cross section is added because – in this theoretical framework – it is treated as a single polarization observable. The term ρ_o is defined as $\rho_o = |\vec{q}|/|\vec{k}|$.

B.1 Single Polarization observables

$$\sigma_o(\theta) = \rho_o \Re\{\ |f_1|^2 + |f_2|^2 - 2\cos\theta\ f_2 f_1^* + \frac{\sin^2\theta}{2}[\ |f_3|^2 + |f_4|^2 + 2f_4 f_1^* + 2f_3 f_2^* + 2\cos\theta\ f_4 f_3^*]\ \} \quad (20)$$

$$P_y(\theta) = \frac{\rho_o \sin\theta}{\sigma_o(\theta)}\ Im\{\ [2f_2 + f_3 + \cos\theta\ f_4]^*\ f_1 + f_2^*\ (\cos\theta\ f_3 + f_4) + \sin^2\theta\ f_3^* f_4\ \} \quad (21)$$

$$\Sigma_x(\theta) = -\frac{\rho_o \sin^2\theta}{2\sigma_o(\theta)}\ Re\{\ |f_3|^2 + |f_4|^2 + 2(\ f_1^* f_4 + f_2^* f_3 + \cos\theta\ f_3^* f_4\ )\ \} \quad (22)$$

$$T_y(\theta) = \frac{\rho_o \sin\theta}{\sigma_o(\theta)}\ Im\{\ f_1^* f_3 - f_2^* f_4 + \cos\theta\ (f_1^* f_4 - f_2^* f_3) - \sin^2\theta\ f_3^* f_4\ \} \quad (23)$$

B.2 Double Polarization Observables

B.2.1 Beam – Target Polarization

$$E(\theta) = \frac{\rho_o}{\sigma_o(\theta)}[|\ f_1\ |^2 + |\ f_2\ |^2\ - Re\{2\cos\theta f_1^* f_2 - \sin^2\theta(f_2^* f_3 + f_1^* f_4)\}] \quad (24)$$

$$F(\theta) = \frac{\rho_o \sin\theta}{\sigma_o(\theta)} Re\{f_1^* f_3 - f_2^* f_4 + \cos\theta(f_1^* f_4 - f_2^* f_3)\} \quad (25)$$

[18] Up to an arbitrary common phase factor.

[19] In principle, one additional experiment is sufficient [21], not two as stated by Barker [53]. Please note that 8 measurements are only sufficient and in case of negligible statistical and systematical errors and if they are selected in such a way that their combination resolves all discrete ambiguities.

$$G(\theta) = -\frac{\rho_o \sin^2\theta}{\sigma_o(\theta)} Im\{f_2^* f_3 + f_1^* f_4\} \tag{26}$$

$$H(\theta) = \frac{\rho_o \sin\theta}{\sigma_o(\theta)} Im\{2f_1^* f_2 + f_1^* f_3 - f_2^* f_4 + \cos\theta[f_1^* f_4 - f_2^* f_3]\} \tag{27}$$

B.2.2 Beam – Recoil Polarization

$$C_{x'}(\theta) = \frac{\rho_o \sin\theta}{\sigma_o(\theta)} Re\{\mid f_2 \mid^2 - \mid f_1 \mid^2 + f_2^* f_3 - f_1^* f_4 + \cos\theta(f_2^* f_4 - f_1^* f_3)\} \tag{28}$$

$$C_{z'}(\theta) = \frac{\rho_o}{\sigma_o(\theta)} Re\{-2f_1^* f_2 + \cos\theta(\mid f_1 \mid^2 + \mid f_2 \mid^2) - \sin^2\theta(f_1^* f_3 + f_2^* f_4)\} \tag{29}$$

$$O_{x'}(\theta) = \frac{\rho_o \sin\theta}{\sigma_o(\theta)}\ Im\{\ f_2 f_3^* - f_1 f_4^* + \cos\theta\ (f_2 f_4^* - f_1 f_3^*)\ \} \tag{30}$$

$$O_{z'}(\theta) = -\frac{\rho_o \sin^2\theta}{\sigma_o(\theta)}\ Im\{\ f_1 f_3^* + f_2 f_4^*\ \} \tag{31}$$

B.2.3 Target – Recoil Polarization

$$L_{x'}(\theta) = \frac{\rho_o \sin\theta}{\sigma_o(\theta)}\{\mid f_1 \mid^2 - \mid f_2 \mid^2 + \frac{1}{2}\sin^2\theta(\mid f_4 \mid^2 - \mid f_3 \mid^2) - f_2^* f_3 + f_1^* f_4 + \cos\theta(f_1^* f_3 - f_2^* f_4)\} \tag{32}$$

$$\begin{aligned} L_{z'}(\theta) = \frac{\rho_o}{\sigma_o(\theta)} Re\{&2f_1^* f_2 - \cos\theta(\mid f_1 \mid^2 + \mid f_2 \mid^2) + \sin^2\theta(f_1^* f_3 + f_2^* f_4 + f_3^* f_4) \\ &+ \frac{1}{2}\cos\theta\sin^2\theta(\mid f_3 \mid^2 + \mid f_4 \mid^2)\} \end{aligned} \tag{33}$$

$$T_{x'}(\theta) = \frac{\rho_o}{\sigma_o(\theta)} Re\{\sin^2\theta[-f_1^* f_3 - f_2^* f_4 - f_3^* f_4 - \frac{1}{2}\cos\theta(\mid f_3 \mid^2 + \mid f_4 \mid^2)]\} \tag{34}$$

$$T_{z'}(\theta) = \frac{\rho_o}{\sigma_o(\theta)} Re\{\sin\theta[f_1^* f_4 - f_2^* f_3 + \cos\theta(f_1^* f_3 - f_2^* f_4) + \frac{1}{2}\sin^2\theta(\mid f_4 \mid^2 - \mid f_3 \mid^2)]\} \tag{35}$$

C Energy Independent Likelihood Analysis

The general idea of likelihood techniques is to perform an energy independent parameterization of the full differential cross sections in terms of physical or pure mathematical meaningful variables. Energy independent likelihood analyses have been used extensively to study meson spectra via several production mechanisms such as peripheral production, central production, J/Ψ radiative decays, and $p\bar{p}$-antiproton annihilations at rest and formations in flight [46]. Meson studies of the past few decades have benefited from a plethora of high quality data. Fortunately, high quality baryon resonance data are becoming attainable, and utilizing the tools developed for meson spectroscopy, will provide additional and complementary techniques for the study of baryon resonances.

C.1 Cross Sections and Accepted Distributions

Often due to limitations in the experimental apparatus, one does not directly measure differential cross sections, but rather one observe "accepted differential cross section", $\tilde{\sigma_a}$. Alternatively, one may discuss the total number of accepted events and its accepted angular intensity rather than total and differential accepted cross sections, that is $\tilde{\sigma_a} \propto N$ and $\frac{\partial \tilde{\sigma_a}}{\partial \tau} \propto I(\tau)$.

$$\tilde{\sigma_a} = \int \frac{\partial \tilde{\sigma_a}}{\partial \tau} \, dLips = \int \frac{\partial \sigma}{\partial \tau} \eta(\tau) \, dLips$$

is the accepted differential cross section. The variable τ represents collectively all the measured variables necessary to have a complete description of the final state. For example, τ may include the set:$\{W, \theta, \phi, p, \theta', \phi', p', \ldots\}$. The experimental acceptance is represented by $\eta(\tau)$, and $dLips$ is the Lorentz-invariant phase space element.

C.2 Accounting for Acceptance

Since the acceptance $\eta(\tau)$ is generally not known analytically, it is often evaluated using MC techniques in which the effects of the experiment are modeled to account for the experimental acceptance. There are in general two ways to handle acceptance. One way involves using MC events to correct for losses in binned distributions. This method can work well for systems with a few measured variables. Often though, correlations among measured variables and model-dependent assumptions can lead to deficient corrections. An alternative approach takes acceptance into account via an extended likelihood analysis. An extended (or generalized) likelihood analysis can be used to determine reaction amplitudes that best describe the data. It is performed by fitting the parameters to maximize the likelihood. A properly normalized likelihood function for finding N_a observed events is

$$\mathcal{L} = e^{-\tilde{\sigma_a}} \prod_i^{N_a} \frac{\partial \tilde{\sigma_a}}{\partial \tau_i}$$

In practice, one minimizes the negative of the log-likelihood:

$$-ln\mathcal{L} = -ln(\prod_i^{N_a} \frac{\partial \tilde{\sigma_a}}{\partial \tau_i}) + \tilde{\sigma_a}$$

One is free to choose any complete set of basis functions to expand the cross section. For instance, a purely mathematical orthonormal basis are the angular moments

$$\frac{\partial \sigma}{\partial \tau} \propto \sum_\alpha h_\alpha H^*_\alpha(\tau).$$

Alternatively, one could choose a physically connected basis as in helicity decay amplitudes, CGLN amplitudes, which are linear combinations of helicity decay amplitudes that are eigenstates of parity, or the traditional E-M multipoles [20, 55].

For example, the cross section expanded in terms of amplitudes ${}^\beta A_\alpha(\tau)$ becomes

$$\frac{\partial \sigma}{\partial \tau} = \sum_{\alpha,\alpha',\beta} {}^\beta A^*_{\alpha'}(\tau)\ {}^\beta \rho_{\alpha'\alpha}(\tau)\ {}^\beta A_\alpha(\tau).$$

The index α refers to interfering amplitudes whereas the index β refers to non-interfering amplitudes, and often β corresponds to external initial and final spin configurations and α refers to a particular $J^P M$.

An energy independent analysis can be performed by binning the data in W. Note that this assumes the energy dependence, and thus a resonance mass dependence, is constant or nearly constant over the bin range. The main advantage of binning in energy is that the spin-density matrix no longer depends on τ and thus can be factored out of the integration.

$$-ln\mathcal{L} = -ln(\prod_i^{N_a} \frac{\partial \tilde{\sigma_a}}{\partial \tau_i}) + \sum_{\alpha,\alpha',\beta} {}^\beta \rho_{\alpha'\alpha} \int {}^\beta A^*_{\alpha'}(\tau)\ {}^\beta A_\alpha(\tau) \eta(\tau) dLips.$$

Since the acceptance $\eta(\tau)$ is not known analytically, the remaining integrals

$${}^\beta \Phi^a_{\alpha'\alpha} = \int {}^\beta A^*_{\alpha'}(\tau)\ {}^\beta A_\alpha(\tau)\ \eta(\tau) dLips$$

do not depend on the parameters of the fit, and they are evaluated using MC events subjected to a simulation of the experimental apparatus:

$${}^\beta \Phi^a_{\alpha'\alpha} = \frac{1}{N_G} \sum_i^{N_a} {}^\beta A^*_{\alpha'}(\tau)\ {}^\beta A_\alpha(\tau)$$

The sum is over the accepted MC event sample where N_G is the number of generated MC events required to achieve a final set of N_a accepted events from the simulations. The phase space factor is taken into account by generating the MC events weighted according to phase space.

After the likelihood fit of the density matrix elements, the acceptance corrected cross sections are readily obtained via

$$\sigma = \sum_{\alpha,\alpha',\beta} {}^{\beta}\rho_{\alpha'\alpha}\, {}^{\beta}\Phi^{a}_{\alpha'\alpha}$$

where

$${}^{\beta}\Phi^{a}_{\alpha'\alpha} = \frac{1}{N_G}\sum_{i}^{N_G} {}^{\beta}A^{*}_{\alpha'}(\tau)\, {}^{\beta}A_{\alpha}(\tau)$$

are integrals over the generated MC sample where these generated MC events are not subjected to a simulation of the experimental apparatus.

The acceptance corrected partial wave cross section for a definite wave α, where α may refer to a particular J^P, is

$$\sigma_{\alpha} = \sum_{\beta} {}^{\beta}\rho_{\alpha\alpha}\, {}^{\beta}\Phi^{a}_{\alpha\alpha}$$

References

[1] R. Koniuk and N. Isgur, Phys. Rev. **D21**, 1868 (1980); N. Isgur and G. Karl, Phys. Lett. **72B**, 109 (1977).

[2] S. Capstick and N. Isgur, Phys. Rev. **D34**, 2809 (1986).

[3] S. Capstick, Phys. Rev. **D46**, 2864 (1992); S. Capstick and W. Roberts, Phys. Rev. **D49**, 4570 (1994).

[4] D.B. Lichtenberg, Phys. Rev. **178**, 2197 (1969); R.E. Cutkosky and R.E. Hendrick, Phys. Rev. **D16**, 2902 (1977).

[5] S. Capstick and W. Roberts, Phys. Rev. **D58**, 074011 (1998); Nucl. Phys. **45, Suppl. 2**, 5241 (2000).

[6] C.L. Schat, J.L. Goity, N.N. Scoccola, hep-ph/0111082 (2001); J.L. Goity, Phys. Lett. **B414**, 140 (1997); C.E. Carlson, C.D. Carone, J.L. Goity, and R.F. Lebed, Phys. Lett. **B438**, 327 (1998), Phys. Rev **D59**, 114008 (1999).

[7] SAPHIR Collaboration: M.Q. Tran *et al.*, Phys. Lett. **B445**, 20 (1998).

[8] T. Mart and C. Bennhold, Phys. Rev. **C61**, 012201 (2000).

[9] B. Saghai *et al.*, in: Proceedings of the *Workshop on Hypernuclear Physics with Electromanetic Probes*, Hampton (VA), Dec. 1999; B. Saghai, invited talk at *International Symposium on Hadrons and Nuclei*, Seoul, Feb. 2001, nucl-th/0105001.

[10] R.L. Anderson *et al.*, Phys. Rev. Letters **9**, 131 (1962); C.W. Peck, Phys. Rev. **135**, 830 (1964); A.J. Sadoff *et al.*, Bull. Am. Phys. Soc. **9**, 23 (1964); R.L. Anderson *et al.*, Proc. Int. Symp. on electron and photon interactions, Hamburg (1965), 203; S. Mori, Ph.D. thesis, Cornell University, 1966; H. Thom, a compilation, Phys. Rev. **151** 1322 (1966); N.B. Mistry *et al.*, Phys. Lett. B **24** 528 (1967); D.E. Groom, J.H. Marshall, Phys. Rev. **159**, 1213 (1967); A. Bleckmann *et al.*, Z. Phys. **239**, 1 (1970); T. Fujii *et al.*, Preprint (INS, Univ. of Tokyo, 1970); P. Feller *et al.*, Nucl. Phys. B **39** 413 (1972); M. Grilli *et al.*, Nuovo Cim. **38** 1467 (1965).

[11] D. Decamp *et al.*, L.A.L. 1236 (1970).

[12] G. Goeing, W. Schorch, J. Tietge, W. Weilenbock, Nucl. Phys. **B26**, 121 (1971).

[13] R. Haas *et al.*, Nucl. Phys. **B137** 261 (1978).

[14] R.L. Anderson *et al.*, Phys. Rev. **D14**, 679 (1976).

[15] K. Abe *et al.*, Phys. Rev. **D32**, 2869 (1985).

[16] SAPHIR Collaboration: W.J. Schwille *et al.*, Nucl. Instrum. and Methods **A344**, 470 (1994).

[17] SAPHIR Collaboration: M. Bockhorst *et al.*, Z. Phys. **C63**, 37 (1994).

[18] SAPHIR Collaboration: S. Goers *et al.*, Phys. Lett. **B464**, 331 (1999).

[19] TJNAF experiment E89-004 (1989): "Electromagnetic Prodcution of Hyperons", spokesperson R. Schumacher.

[20] G.F. Chew, M.L. Goldberger, F.E. Low, and Y. Nambu, Phys. Rev. **106**, 1345 (1957).

[21] W.-T. Chiang, F. Tabakin, Phys. Rev. **C55**, 2054 (1997).

[22] G. Knöchlein, D. Drechsel, and L. Tiator, Z. Phys. **A352**, 327 (1995).

[23] C.G. Fasano, F. Tabakin, B. Saghai, Phys. Rev. **C46**, 2430 (1992).

[24] R.A. Adelseck, C. Bennhold, L.E. Wright, Phys. Rev. **C32**, 1681 (1985); R.A. Adelseck and B. Saghai, Phys. Rev. **C42**, 108, 1990.

[25] R.A. Williams, C-R. Ji, S.R. Cotanch, Phys. Rev. **C46**, 1617 (1992).

[26] T. Mart, C. Bennhold, C.E. Hyde-Wright, Phys. Rev. **C51**, 1074 (1995).

[27] J.C. David, C. Fayard, G.H. Lamot, B. Saghai, Phys. Rev. **C53**, 2613 (1996).

[28] S.S. Hsiao, D.H. Lu, S.N. Yang, Phys. Rev. **C61**, 068201 (2000).

[29] S. Janssen, J. Ryckebusch, D. Debruyne, and T. Van Cauteren, Phys. Rev. **C65**, 015201 (2001).

[30] T. Feuster and U. Mosel, Phys. Rev. **C58**, 457 (1998); Phys. Rev. **C59**, 460 (1999).

[31] T. Sato and T.-S.H. Lee, Phys. Rev **C54**, 2660 (1996).

[32] W.-T. Chiang, F. Tabakin, T.-S.H. Lee, B. Saghai, Phys. Lett **B517**, 101 (2001).

[33] C. Bennhold, T. Mart, A. Waluyo, H. Haberzettl, G. Penner, T. Feuster, and U. Mosel, in *Proceedings of the Workshop on Electron Nucleus Scattering*, Elba, Italy, 1998, nucl-th/9901066 (1999); H. Haberzettl, C. Bennhold, T. Mart and T. Feuster, in *Proceedings of Baryons 98*, Bonn, Germany, 1998, nucl-th/9811024 (1998).

[34] D.H. Saxon *et al.*, Nucl. Phys. **B162**, 522 (1980).

[35] K.W. Bell *et al.*, Nucl. Phys. **B222**, 389 (1983).

[36] G. Niculescu *et al.*, Phys. Rev. Lett. **81**, 1805 (1998).

[37] C. Bennhold, H. Haberzettl, T. Mart, invited talk at the *2nd ICTP International Conference on Perpectives in Hadronic Physics*, Trieste Italy, June 1998, nucl-th/9909022 (1999).

[38] B. Saghai, Nucl. Phys. **A639**, 217c (1998).

[39] Z. Li, B. Saghai, Nucl. Phys. **A644**, 345 (1998); Z. Li, B. Saghai, T. Ye, Q. Zhao, *work in progress.*

[40] Z. Li, H. Ye, M. Lu, Phys. Rev **C56**, 1099 (1997).

[41] F.X. Lee, T. Mart, C. Bennhold, H. Haberzettl, L.E. Wright, nucl-th/9907119.

[42] R. A. Arndt, I. I. Strakovsky, and R. L. Workman, work in progress, cf. http://gwdac.phys.gwu.edu.

[43] D. A. Jenkins and I. I. Strakovsky, Phys. Rev. **C52**, 3499 (1995).

[44] R. A. Arndt, C. H. Oh, I. I. Strakovsky, R. L. Workman, and F. Dohrmann, Phys. Rev. **C56**, 3005 (1997).

[45] M. Guidal *et al.*, Nucl. Phys. **A627** 645 (1997); M. Guidal, J. M. Laget, and M. Vanderhaegen, Phys. Rev. **C61**, 025204 (2000).

[46] See for example: S.U. Chung *et al.*, Phys. Rev. **D65**, 072001 (2002); C. Amsler, Nucl. Phys. **A663**, 93 (2000).

[47] W. Meyer, in *Proceedings of the GDH2000 Symposium* Mainz, Germany, 2000, (World Scientific, 2001) p. 157.

[48] Y. Miyachi, in *Proc. 8th Int. Workshop on Polarized Materials and Techniques*, Vancouver, Canada, 1996; SPring8 proposal 2001, “The test of the GDH sum rule at SPring8”, spokesperson T. Iwata, Nagoya, Japan; T. Iwata, N. Horikawa, *private communication.*

[49] D.G. Crabb and W. Meyer, Ann. Rev. Nucl. Part. Sci. **47**, 67 (1997).

[50] H. Dutz *et al.* , NIM **A356**, 111 (1995).

[51] K. Livingston *et al.*, Internal CLAS-Report, Nov. 2000.

[52] TJNAF experiment E01-104 (2001): "Helicity Structure of Pion Photoproduction", update of E91-015, spokespersons D. I. Sober, M. Khandaker, D. G. Crabb.

[53] I.S. Barker, A. Donnachie, J.K. Storrow, Nucl. Phys. **B75**, 347 (1975).

[54] G. Keaton and R. Workman, Phys. Rev. **C53**, 1434 (1996).

[55] R.L. Walker, Phys. Rev. **182**, 1729 (1969).